

5-1-2014

Targeted Cancer Nanotherapeutics by Adoptive Transfer of Mononuclear Splenocytes

Jaclyn Murton

Follow this and additional works at: https://digitalrepository.unm.edu/biom_etds

Recommended Citation

Murton, Jaclyn. "Targeted Cancer Nanotherapeutics by Adoptive Transfer of Mononuclear Splenocytes." (2014).
https://digitalrepository.unm.edu/biom_etds/81

This Thesis is brought to you for free and open access by the Electronic Theses and Dissertations at UNM Digital Repository. It has been accepted for inclusion in Biomedical Sciences ETDs by an authorized administrator of UNM Digital Repository. For more information, please contact disc@unm.edu.

Jaclyn Murton
Candidate

Biochemistry and Molecular Biology & Cell Biology and Physiology
Department

This thesis is approved, and it is acceptable in quality and form for publication:

Approved by the Thesis Committee:

Dr. Helen Hathaway, Chairperson

Dr. Natalie Adolphi, Mentor

Dr. Judy Cannon

**TARGETED CANCER NANOTHERAPEUTICS BY
ADOPTIVE TRANSFER OF MONONUCLEAR
SPLENOCYTES**

by

JACLYN MURTON

**B.S. BIOLOGY, UNIVERSITY OF NEW MEXICO,
2005**

THESIS

Submitted in Partial Fulfillment of the
Requirements for the Degree of

**Masters
Biomedical Sciences**

The University of New Mexico
Albuquerque, New Mexico

May 2014

ACKNOWLEDGEMENTS

I thank Dr. Natalie Adolphi, my advisor, for guiding me through my thesis project and manuscripts. Her guidance and professional style will remain with me as I continue my career. I also thank my committee members, Dr. Helen Hathaway and Dr. Judy Cannon, for their valuable recommendations pertaining to this study and assistance in my professional development. I would also like to thank my fellow lab mates, Chelin Hu, Sara Alcon, Mona Ahmed, Nancy Orduno, Lauren Marek and Eric Joseph who were instrumental in guiding me the scientific process. I sincerely appreciate Tamara Howard's guidance and mentorship regarding designing and analyzing many of my experiments. Gratitude is extended to the UNM Cancer Center and the University of New Mexico School of Medicine for the funding to pursue this research. I would like to thank Dr. Norenberg and the KUSAIR staff for assisting with the SPECT imaging, Dr. Orlando's group for guidance on cell harvesting techniques, and the Flow Cytometry Core Facility for assistance on instrumentation and data processing.

Additional appreciation goes towards Sandia National Laboratories for making it possible for me to participate in the Biomedical Sciences Graduate Program. A special thanks to Dr. Eric Carnes and Dr. Carlee Ashley for their strong support for this work both financially and collaboratively. Finally, thank you to Dr. James Carney, my department manager at Sandia National Laboratories, for your guidance and support of me throughout my thesis project.

TARGETED CANCER THERAPEUTICS BY ADOPTIVE TRANSFER OF MONONUCLEAR SPLENOCYTES

by

JACLYN MURTON

B.S. BIOLOGY, UNIVERSITY OF NEW MEXICO, 2005

ABSTRACT

The most common cause of cancer deaths among women is breast cancer. Current breast cancer chemotherapies rely on passive diffusion of the drug into the tumor interior, which leads to a sub-optimal drug concentration in some tumor regions. One important goal for cancer pharmaceuticals is optimizing drug targeting to tumors. We propose to develop active drug delivery, mediated by the patient's immune cells. We hypothesize that circulating monocytes, known to infiltrate tumors, are effective biologically-active carriers of multifunctional nanoparticles. Peripheral blood mononuclear cells (MS) were isolated from the spleens of transgenic mice that are immunocompetent and spontaneously develop mammary tumors. We demonstrate that MS remain viable after being loaded with a nanoparticle cargo (protocells). The protocell biodistribution was assessed in vivo by radioimaging of tumor-bearing and normal mice injected with protocell-loaded MS, and demonstrated a preferential accumulation of protocells in tumor relative to normal mammary tissue.

TABLE OF CONTENTS

LIST OF FIGURES	ix
LIST OF TABLES	xi
LIST OF ABBREVIATIONS	xii
CHAPTER 1 INTRODUCTION	1
1.1 Purpose of the Study	1
1.2 Hypothesis.... ..	1
1.3 Significance.....	1
CHAPTER 2 REVIEW OF RELATED LITERATURE.....	2
2.1 Challenges in Breast Cancer	2
2.2 Pathophysiology of Breast Cancer	4
2.3 Therapeutic Strategies	5
2.4 Protocells.....	9
2.5 Tumor Immunology	10
2.6 Immune Cell Mediated Delivery of Cancer Therapeutics	11
2.7 Immune-Competent Mouse Model of Breast Cancer	12
CHAPTER 3 ISOLATION AND CHARACTERIZATION OF POTENTIAL IMMUNE CELL CARRIERS.....	16
3.1 Introduction.... ..	16
3.2 Methods.....	17
3.2.1 Establishment of PyMT Mice	17
3.2.2 Extraction of Mononuclear Immune Cells from Spleen..	17
3.2.3 Purification of Mononuclear Splenocytes.....	18

3.2.4 Preparation of Bone Marrow Derived Macrophages (BMDM).....	19
3.2.5 Morphological Analysis of MS and BMDM	19
3.2.6 Phenotypic Analysis of MS and BMDM.....	20
3.2.7 Phagocytic Capacity of MS and BMDM.	21
3.3 Results.....	22
3.3.1 Viability and Morphology of MS and BMDM.....	22
3.3.2 Phenotype of MS and BMDM.....	24
3.3.3 Phagocytic Capacity of MS and BMDM	25
CHAPTER 4 IN VIVO BIODISTRIBUTION OF MS AND BMDM	29
4.1 Introduction....	29
4.2 Methods.....	29
4.2.1 SPECT/CT Imaging of MS and BMDM Biodistribution ..	29
4.2.2 Quantitative Analysis of SPECT/CT Image Data	31
4.2.3 Activation of MS versus Incubation Time at 37°C	31
4.2.4 Effect of Incubation at 37°C on MS Phenotype and Phagocytosis.....	32
4.2.5 Demonstrating Tumor Infiltration of Cargo-Loaded MS .	33
4.2.6 Purification of Myeloid-Derived Stem Cells from MS.....	33
4.3 Results.....	34
4.3.1 SPECT/CT Imaging of MS and BMDM Biodistribution .	34
4.3.2 Activation of MS versus Incubation Time at 37°C	40
4.3.3 Effect of Incubation at 37°C on MS Phenotype and	

Phagocytosis.....	42
4.3.4 Confirmation that Cargo-Loaded MS Infiltrate Tumors ..	44
4.3.5 Purification of Myeloid-Derived Stem Cells (MDSC)	
from MS.....	45
CHAPTER 5 IN VIVO BIODISTRIBUTION OF PROTOCELL-LOADED MS AND	
 BMDM	47
5.1 Introduction.....	47
5.2 Methods.....	47
5.2.1 Protocell Formulation	47
5.2.2 MS Protocell Uptake and Cytotoxicity Analysis	49
5.2.3 <i>In vivo</i> Comparison of Protocell Loaded MS	
Biodistribution by Protocell Formulation	50
5.2.4 SPECT/CT Imaging of DOPC-DOPS Protocell	
Biodistribution after Direct Injection, MS Adoptive Transfer	
and BMDM Adoptive Transfer.....	51
5.3 Results.....	53
5.3.1 Optimization of MS Protocell Uptake and Viability	53
5.3.2 Biodistribution of Different Protocell Formulations after Direct	
Injection versus MS Adoptive Transfer	55
5.3.3 SPECT/CT Imaging of DOPC-DOPS Protocell	
Biodistribution after Direct Injection, MS Adoptive Transfer,	
and BMDM Adoptive Transfer	57
CHAPTER 6 DISCUSSION	72

6.1 Introduction.....	72
6.2 Discussion of Results and Conclusions.....	74
6.3 Recommendations for Further Research	82
APPENDICES.....	83
LITERATURE CITED	84

LIST OF FIGURES

Figure 1. Density Gradient Isolation of Mononuclear Splenocytes (MS)	23
Figure 2. Morphology of Density Gradient Separated (MS) and Bone Marrow-Derived Macrophages (BMDM).....	23
Figure 3. MS and BMDM Expression of Myeloid-like Receptors	25
Figure 4. MS Phagocytosis of PKH26 Cytotracker	27
Figure 5. BMDM Phagocytosis of 1 μ m Latex Beads	28
Figure 6. Biodistribution of Radiolabeled MS in PyMT Mice after 30min.....	35
Figure 7. Biodistribution of Radiolabeled MS in PyMT Mice after 5 hrs	
Figure 8. Biodistribution of Radiolabeled MS in PyMT Mice after 24 hrs	37
Figure 9. Region of Interest (ROI) Analysis of SPECT/CT Images of MS Biodistribution	
Figure 10. Biodistribution of Radiolabeled BMDM.....	40
Figure 11. Cytokine Array of Pre-Injected MS	42
Figure 12. Biodistribution Sample Condition Analysis	43
Figure 13. Biodistribution of Sample Condition Analysis	44
Figure 14. Biodistribution of PKH26 Loaded MS	45
Figure 15. Purification of MDSC from the MS Population	46

Figure 16. Fraction and Viability of MS Loaded with	
Protocells.....	54
Figure 17. Biodistribution of Protocell Loaded MS	56
Figure 18. Visual Confirmation of Protocell Delivery to Tumors	57
Figure 19. Biodistribution of MS Loaded with DOPC-DOPS	
Protocells	59
Figure 20. Quantitative Confirmation of MS-mediated DOPC-DOPS	
Protocell Biodistribution	60
Figure 21. Biodistribution of Directly Injected DOPC-DOPS	
Protocells.....	61
Figure 22. Biodistribution of BMDM Loaded with DOPC-DOPS	
Protocells	63
Figure 23. SPECT/CT Analysis of Protocell Delivery to	
Tumor/mammary Tissue	65
Figure 24. SPECT/CT Analysis of Protocell Delivery to Liver.....	66
Figure 25. SPECT/CT Analysis of Protocell Delivery to Kidneys.....	67
Figure 26. SPECT/CT Analysis of Protocell Delivery to Spleen	68
Figure 27. SPECT/CT Analysis of Protocell Delivery to Lungs.....	69
Figure 28. SPECT/CT Analysis of Protocell Delivery to Bones	70
Figure 29. SPECT/CT Analysis of Protocell Delivery to Heart.....	71

LIST OF TABLES

Table 1. DOPC-PEG Uptake Tolerance	85
Table 2. DOPC-DOTAP Uptake Tolerance	85
Table 3. DOPC-DOPS Uptake Tolerance	85

LIST OF ABBREVIATIONS

%ID/g	Percent Injected Dose per Gram of Tissue
ANOVA	Analysis of Variance
BMDM	Bone Marrow Derived Macrophages
CM	Circulating Monocyte
CSF-1	Colony Stimulating Factor-1
DAPI	4',6-Diamidino-2-phenylindole, dilactate
DCIS	Ductal Carcinoma <i>in situ</i>
DMEM	Dulbecco's Modified Eagle's Medium
DOPC	1,2-Dioleoyl-sn-glycero-3-phosphocholine
DOPS	1,2-Dioleoyl-sn-glycero-3-phosphoserine
DOTAP	n-(1-(2,3-dioleoyloxy)propyl)-N,N,N-trimethylammonium methylsulfate
EPR	Enhanced Permeability and Retention
HBSS	Hank's Balanced Salt Solution
IV	Intravenous
LCIS	Lobular Carcinoma <i>in situ</i>
LT	Large tumor antigen
MDSC	Myeloid-derived Suppressor Cells
MMTV	Mouse Mammary Tumor Promoter
MMTV-LTR	Mouse mammary tumor virus long terminal repeat
MT	Middle tumor antigen
OCT	Optimal Cutting Temperature Compound

PBS	Phosphate Buffered Saline
PEG	Polyethylene Glycol
PFA	Paraformaldehyde
PyMT	polyomavirus middle T antigen
PyV	Polyoma virus
ROI	Region of Interest
RPMI	Roswell Park Memorial Institute Medium
SPECT	Single-Photon Emission Computed Tomography
SRC-1	Steroid Receptor Coactivator-1
ST	Small tumor antigen
TAM	Tumor associated macrophage
WGA	Wheat Germ Agglutinin

Chapter 1

Introduction

1.1 PURPOSE OF THE STUDY

The purpose of this study is to develop a method of active delivery involving loading immune cells with therapeutic nanodrugs. We will identify and characterize phagocytic tumor infiltrating immune cells as cargo carriers for breast cancer treatment in a mouse model for breast cancer.

1.2 HYPOTHESIS

We hypothesize that tumor infiltrating monocytes are effective biologically-active carriers of multifunctional nanoparticles.

1.3 SIGNIFICANCE

Improvement of drug targeting to tumors will significantly diminish the unpleasant side effects of chemotherapy by reducing the systemic exposure to chemotherapeutics and the concentration required to elicit an effective tumor dose. Immune cell carriers might also prolong the half-life of drugs that are susceptible to environmental factors.

Chapter 2

Review of Related Literature

2.1 CHALLENGES IN BREAST CANCER

Invasive breast cancer accounts for 23% of all cancers in women globally and is the most common carcinoma diagnosed in women. The highest incidence of breast cancer occur in affluent populations in Australia, Europe and North America (Lakhani 2012). In 2012, the World Health Organization identified a sharp rise in breast cancer worldwide. The incidence of breast cancer diagnoses increased by 20% since 2008 and the mortality rate increased by 14%. The most common cause of cancer related mortalities among women is through complications with breast cancer (Terrassee 2013).

Cancers are challenging to diagnose and often require invasive therapies such as surgery, chemotherapy, hormone therapy, and targeted therapy. Invasive cancers require more aggressive treatment strategies that result in uncomfortable side effects like hair loss, nausea, low blood cell counts, neuropathy, and heart damage (Bae 2011). The physiology of breast tissue renders it particularly susceptible to cancer. The mammary gland epithelium is highly dynamic and undergoes dramatic changes in response to the hormonal changes of normal female development and pregnancy (Visvader 2009). The developmental stage of breast cells is dependent on the maturity of the woman and whether or not she has had a full-term pregnancy. Epidemiological studies strongly suggest that androgens, estrogens, and progesteogens play an

important role in the development of carcinomas (Lakhani 2012). The hormone estrogen stimulates cell division in response to the various developmental and reproductive requirements throughout a woman's lifespan, increasing the risk of permanent DNA damage (Nakada 2014). Immature breast cells tend to bind more carcinogens and are less effective at repairing DNA damage compared to mature cells. Most breast development occurs between puberty and a woman's first pregnancy, which is why the risk of breast cancer is increased in women who have not had a full-term pregnancy before 35 years of age (Russo 1982). After a woman's first full-term pregnancy, the majority of immature stem cells transform into differentiated milk producing cells, which are less sensitive to DNA damage (Visvader 2009). Also, cancer is more likely to occur in tissues with immature cells that are rapidly dividing, so the risk of carcinogenesis goes down as more immature stem cells differentiate.

In addition to the susceptibility of breast tissue towards cancerization, the physiological architecture of the breast intensifies the risk of metastasis. The breast is an interconnected network of ducts and lobes accessible to the lymphatic system, which allows transformed cells easy access to the rest of the body. The risk of developing inflammatory carcinomas is also increased in breast tissue due to the close proximity of the lymphatic network and invasive ductal carcinomas account for roughly 80% of breast cancer diagnoses (Siziopikou 2013).

2.2 PATHOPHYSIOLOGY OF BREAST CANCER

Combating breast cancer requires an understanding of the pathophysiology of the disease. Breast cancer is traditionally subdivided into four main types: two non-invasive and two invasive cancers. The two noninvasive, or *in situ*, cancers are ductal carcinoma *in situ* (DCIS) and lobular carcinoma *in situ* (LCIS). DCIS accounts for 20% of breast cancer diagnoses and involves epithelial transformation towards malignancy, though confined within the basement membrane (Siziopikou 2013). The less commonly diagnosed LCIS is a noninvasive lesion found in and confined to lobules and terminal ducts (Afonso 2008). The invasive forms of breast cancer are referred to as infiltrating ductal and lobular carcinomas and are the second most common type of breast cancer, accounting for up to 14% of cases (Harake 2001). In both cases, cellular proliferation escapes the wall of the duct or lobule. The severity of the four main types of breast cancer is categorized by four stages of development. Healthy breast tissue ducts and lobules are subdivided into terminal ductal lobular units that contain ducts and lobules composed of a bi-layered epithelium consisting primarily of luminal and myoepithelial cells. In the initial stages of carcinoma development, abnormal cell layers begin to proliferate within the duct or lobule forming a premalignant lesion called an atypical ductal hyperplasia. These *in situ* cancers are considered "Stage 0" because the transformed cells are contained within the basement membrane of the tissue (Vargo-Gogola 2007). If cellular proliferation exceeds two centimeters the cancer has progressed to "Stage I". As control of proliferation, survival and differentiation becomes

deregulated, the surrounding stroma becomes more aberrant. The proliferating cells begin to invade the basement membrane and proliferate throughout the surrounding tissue. Once the tumor spreads to the lymph nodes, but remains between two and five centimeters in size it is considered "Stage II". A tumor greater than five centimeters and spreading to the lymph nodes under the arms is considered "Stage III". Tumor metastases are achieved once tumor cells begin to enter the vasculature, surviving in the absence of adhesion, and can exit the vasculature to establish a new tumor microenvironment. This is considered the fourth and final stage of breast cancer (MD Consult 2000).

2.3 THERAPEUTIC STRATEGIES

Mammography, combined with histological sampling of core biopsies and fine-needle aspiration cytology, is the primary imaging method for detection of breast cancer in women over 40 years old. Invasive breast cancer is difficult to definitively diagnose with mammography alone, so ultrasound is often used to improve specificity. Magnetic resonance imaging is the most sensitive method for detecting breast cancer, but is reserved for high risk cases due to the expense (Lakhani 2012).

Therapeutic responses to breast cancer are complicated by the heterogeneity of the disease (Lakhani 2012). There is a significant level of diversity of tumor types both within the disease and between individuals due to the multiplicity of neoplasms that can arise from ductal epithelial cells. Cellular diversity, as influenced by genetic and epigenetic alterations along with adaptive responses

to activated signaling pathways, may occur within tumors. This would explain the diversity of breast tumor subtypes as being composed of different populations of cancer cells. Traditional pathology driven classification has transitioned more towards molecular based classifications to account for the heterogeneity of cancer cell phenotypes combined with the dynamic plasticity of the tumor microenvironment. Further complicating treatment strategies, clonal composition and cellular phenotypes are constantly changing as the tumor environment changes, making tumor biology more of a moving target (Polyak 2011).

The considerable range and complexity of molecular events contributing to carcinogenesis elevates cancer to key research status among several institutions in academia, industry, and non-profit groups. The National Cancer Institute alone had a budget of \$4.8 billion for fiscal year 2013 (Varmus 2013). Though there are several approaches to mitigating cancer, treatment customarily focuses on cytotoxic compounds that have a narrow therapeutic index and high dose-limiting toxicity. Effective treatment often requires the dosage to approach the maximum tolerated levels of the drug, resulting in a demanding regimen for the patient to tolerate. Efforts toward alleviating impact on the patient have diverged into two primary approaches, including finding ways to lower the systemic dose while maximizing the targeted dose or finding alternatives to chemotherapeutics. This work focuses on improving targeted delivery of chemotherapeutics.

The concept of targeting drugs to specific cell types was first developed by Paul Ehrlich in the 1890's. Also the founder of chemotherapy, Ehrlich believed we could learn how to "aim chemically" as a targeted approach to treating

disease. He famously coined the phrase "magic bullet" when suggesting using small molecules to uniquely target cancer cells (Strebhardt 2008). Ehrlich's ideas have inspired the cancer pharmaceuticals community. Several strategies have developed towards reaching specific cancer targets. Advances in nanotechnology and biotechnology contributed the development of engineered nanomaterials for targeted therapies (Sanna 2014). Synthetic nucleic acid ligands, called aptamers, show promise for targeted oligonucleotide based therapies (Dassie 2013). Antibodies and other ligands are classic tools for cancer treatment and immune modulation (Sliwkowski 2013). Other vehicles for drug delivery that have emerged include microbubbles, liposomes, and micelles, which encapsulate the drug as it passively circulates towards the intended target (Zhou 2013).

Though significant progress has been made in drug delivery, there are still substantial challenges to overcome concerning treating solid tumors. Overcoming these obstacles requires an understanding of the *in vivo* dynamics of intravenous (IV) drug transport. Drug targeting strategies are traditionally divided into two approaches: active or passive targeting. Passive targeting capitalizes on the enhanced permeability and retention (EPR) effect whereby the leaky vasculature and poor lymphatic drainage of tumors encourages accumulation of macromolecules or nanoparticles in the tumor interstitium. Tumor cells stimulate angiogenesis in order to supply sufficient oxygen and nutrients to support cellular proliferation. The imbalance of pro and anti-angiogenic signaling that arises results in an abnormal vascular network of

dilated blood vessels with disorganized branching. Though not a targeted therapeutic approach, this strategy relies on the propensity for macromolecular therapeutics to accumulate in the tumor interstitium more prevalently than in normal tissue, thus facilitating a 20-30% larger effective dose in tumors compared to normal tissue (Kobayashi 2014). However the significant heterogeneity of tumor types with respect to vascular pore dimension and vascular architecture limits the predictability of clinical outcomes and the heterogeneous blood flow within a tumor prevents a homogeneous exposure of the drug within the tumor (Prabhakar 2013; Kobayashi 2014). Though the leaky vasculature enables macromolecules to infiltrate the tumor stroma, it also contributes to an increase in interstitial fluid pressure, which offsets extravasation from the blood vessel into tumors and compresses blood vessels such that blood is diverted from the center of the tumor towards the periphery (Kobayashi 2014).

One approach to active targeting requires specific interactions between the drug and the target cell, typically through a ligand-receptor interaction. However, the affinity range of ligand-receptor interactions is less than 15 nm (Leckband 2000). Therefore, ligand-receptor interactions are effective for enhancing retention after the drug enters the tumor, but the ligand-receptor affinity range is too small to facilitate deeper penetration into the tumor from the blood vessel entry point. This strategy might be better described as “targeted retention” rather than “targeted delivery.” Another limitation to ligand-mediated active targeting for cancer therapeutics is the heterogeneity of the cancer cell population. The fraction of tumor cells expressing a specific receptor at any given time is typically

not known, so the ligand-targeted drug is not necessarily targeting all cancer cells within a tumor (Bae 2011).

2.4 PROTOCELLS

Advances in nanomaterials and materials science have opened the doors for optimizing drug delivery to tumors. Nanomaterials are conveniently versatile such that size, charge, surface coating, and composition can be modified. Collaborative efforts towards addressing the multiple challenges to drug delivery at the Advanced Materials Laboratory in Albuquerque, New Mexico have successfully merged liposome technology with materials science to develop a multicomponent lipid-bilayer-coated nanoporous particle capable of carrying various types of cargo for cancer therapeutics. Liposomes were fused to a spherical nanoporous silica core, forming a supported lipid bilayer that can be used as a novel nanocarrier construct, which can be modified with targeting or fusogenic peptides and polyethylene glycol (Ashley 2011). These nanocarriers, called protocells, are designed to enhance the effective dose, selectivity and stability of cancer therapeutics. The high surface area of the nanoporous silica core increases the capacity for therapeutic agents compared to liposomes of similar size. The lipid bilayer is supported by the silica core both structurally and by charge, making the bilayer more stable than liposomes. Protocells are designed to bind with high affinity to cancer cells, become internalized by receptor-mediated endocytosis and release their cargo in the cytosol upon endosome acidification. The cargo is then released into the cytoplasm or

nucleus of the cancer cell, causing cell death (Ashley 2011). Protocells are impressive tools for drug delivery that resolve the issue of protecting the drug during transport, concentrating the effective dose, and providing a mechanism of controlled release. However, protocells remain susceptible to the common obstacles of other targeted therapeutics in that their targetability is limited to the affinity range of surface ligands. Therefore, protocells still must extravasate and passively diffuse through the tumor to reach all targets. Developing a means of active delivery will significantly enhance the performance of protocells and other multimodal delivery platforms.

2.5 TUMOR IMMUNOLOGY

The immune system plays two roles in cancer development and progression. Innate and adaptive immune cells eradicate malignant cells that are marked for destruction by cytotoxic T cells or display signs of apoptosis. Cancer cells, on the other hand, are adept at employing the wound healing dimension of the immune system to promote tumor growth and metastasis (Gutkin 2014). Macrophage presence is increased in tumors compared to healthy tissue and are a major component of leukocyte infiltration in many types of malignant tumors (Talmadge 2007). M1 macrophages predominantly express the killer phenotype and are largely found in tumor islets, while tissue repairing M2 macrophages are present in tumor stroma. Not all tumor associated immune cells are fully differentiated. Myeloid-derived suppressor cells (MDSC) are immature immune cells that accumulate in blood, lymph nodes, bone marrow

and tumor sites of cancer patients and are thought to play a role in suppressing immune response (Gutkin 2014). Cancer patients typically have significantly higher numbers of MDSCs, though the frequency of MDSC subsets differs among cancer types. A subset of MDSCs that express neither monocytic nor granulocytic markers has been found in the blood of patients with breast cancer, and the frequency of MDSCs appears to correlate with tumor burden (Solito S. 2011). These mobile phagocytic and tumor associated immune cells offer a unique opportunity for targeted drug delivery.

2.6 IMMUNE CELL MEDIATED DELIVERY OF CANCER THERAPEUTICS

Several research groups are investigating ways to engage immune cells in the active delivery of therapeutics. Choi et al. developed a photoinduceable therapy using gold nanoshells with peripheral blood monocytes who function as Trojan Horses for drug delivery to solid tumors. Their idea is based on the observation that macrophages may comprise up to seventy percent of the tumor mass. Peripheral blood monocytes will differentiate into tumor associated macrophages (TAM) once they cross the endothelial basement membrane (Choi 2007). Cells of the mononuclear phagocytic system are of particular interest to liposome drug delivery groups due to their plasticity, phagocytic capacity, and natural affinity towards migrating to tumors (Kelly 2011). For example, human monocytes were successfully labeled with superparamagnetic iron oxide nanoparticles to evaluate potential for magnetic resonance detection and potential hyperthermic delivery (Engberink 2007).

2.7 IMMUNE-COMPETENT MOUSE MODEL OF BREAST CANCER

Drug delivery research typically starts with *in vitro* studies to test the targeted delivery strategy being examined and measure the concentration needed to inhibit 50% of cellular growth. However the scope of *in vitro* experiments is limited because the experimental model does not adequately reflect the clinical scenario, making it difficult to predict therapeutic efficacy in clinical settings. *In vivo* testing is more representative of the clinical disease and is usually done in xenograft models, which are immunosuppressed genetically modified mice that are designed to allow injected human cancer cells to develop into xenograft tumors (Bae 2011). Xenograft models are not ideal for testing immune based cancer therapies since they do not have a functioning immune system. Therefore, all *in vivo* investigations in this study were conducted in an immunocompetent MMTV-PyMT transgenic mouse model of breast cancer that expresses activated polyomavirus middle T antigen with a mouse mammary tumor virus promoter (MMTV-PyMT) resulting in spontaneous mammary tumor development by approximately 10 weeks of age.

Murine polyoma virus (PyV) causes tumor formation in a variety of cell types. Three main PyV oncoproteins, the large (LT), middle (MT), and small tumor antigens (ST), are known to contribute to neoplastic transformation. The middle tumor antigen is vital for tumorigenesis after viral infection. A membrane associated protein, MT recruits tyrosine kinases to Src family signaling molecules for downstream regulation of viral DNA replication and RNA transcription (Fluck 2009). MT expression under the control of the MMTV promoter is restricted to

the mammary epithelium where it induces several signaling pathways, such as ras and phosphoinositide-3-kinase (PI3K), which are commonly affected in human breast cancer and lead to the development of metastatic carcinomas (Lin 2003). In the current study, FVB mice were genetically modified to express the PyMT oncoprotein in mammary epithelial cells of female mice using a mouse mammary tumor virus long terminal repeat promoter (MMTV-LTR). The MMTV promoter is hormonally regulated. MMTV-LTR promoters typically cause transgene expression throughout the ductal tree of the mammary (Vargo-Gogola 2007). Tumor development progresses from hyperplasia, as early as four weeks of age, to adenoma/mammary intraepithelial neoplasia, carcinoma *in situ*, at around 10 weeks, and finally to invasive carcinoma which is correlated with the development of pulmonary metastases at approximately 14 weeks of age (Fluck 2009).

MMTV-PYMT mice are excellent models of human breast cancer because this model mimics four distinct stages of tumor progression from premalignant to malignant that are comparable to tumor progression in human breast cancer. In addition to the similar pathophysiology, PyMT tumors express similar biomarkers found in breast tumors associated with poor outcome, such as low estrogen and progesterone receptor expression (Lin 2003). This mouse model has contributed insights into the mechanisms that regulate cell growth and the impact of deregulated cell growth on the tumor microenvironment. Studies on polyomavirus mouse models have illuminated the role of tyrosine phosphorylation, PI3K and p53 in cellular transition to carcinogenesis (Fluck

2009). Knockout studies of steroid receptor coactivator-1 (SRC-1), whereby SRC-1^{-/-} mice were backcrossed with FVB mice and cross-bred with PyMT mice, clarify the link of SRC-1 to tumor metastasis as a loss of SRC-1 expression suppresses breast cancer metastases in PyMT mice (Wang 2009).

The PyMT mouse model exhibits similar tumor inflammatory responses observed in malignant breast tumors (Lin 2003). A large portion of the leukocytes that infiltrate PyMT tumors are macrophages. Several aspects of macrophage-epithelial cell interactions have been well characterized in PyMT tumors. Macrophages are recruited to premalignant hyperplastic lesions in PyMT mammary tumors by colony stimulating factor-1 (CSF-1) overexpression, just before the angiogenic switch that leads to malignancy (Lewis 2006). These TAMs accelerate vascularization of the lesions, which enhances tumor growth and facilitates progression towards malignancy. During tumor formation, TAMs tend to accumulate in hypoxic and necrotic areas, which appear to inhibit further migration, thus immobilizing the macrophages in these regions. TAMs mitigate to hypoxic environments by up-regulating transcription factors and other proangiogenic factors to increase oxygen flow. The extensive involvement of macrophages in vessel formation and remodeling in hypoxic regions of tissue makes macrophages key modulators of angiogenesis (Lewis 2006).

Although MMTV-PyMT mice are excellent models of human breast cancer, there are a few differences to consider. MT tumors primarily metastasize to the lung, whereas human metastases are more broadly distributed to the brain, lungs, bones and liver. The MMTV promoter facilitates MT expression

throughout the ductal tree, which does not mimic oncogene expression in a more limited number of cells in human tumors. Expression levels of the MT oncogene are likely higher than oncogenic expression in human tumors. Also, the MMTV promoter may not target all of the same progenitor cell types that are involved in human breast cancer tumor formation (Fluck 2009).

Chapter 3

Isolation and Characterization of Potential Immune Cell Carriers

3.1 INTRODUCTION

The heterogeneous cell types involved in an inflammatory response to tumor development suggests a broad spectrum approach towards identifying potential immune cell carriers for therapeutic delivery. Circulating immature myeloid cells are strong candidates for drug transport because they naturally extravasate from the bloodstream into tissue stroma to scavenge toxic compounds and remove apoptotic cells, demonstrating phagocytic capacity (Auffray 2009). Myeloid cells are often associated with the tumor stroma and microenvironment and can be enriched from the patient's blood, lymph nodes and bone marrow (Gutkin 2014). Myeloid cells comprise 53-86% of leukocytes in normal human blood and are known to expand in breast cancer as monocytes, which function as a reservoir of precursor innate immune cells, and are recruited to the tumor by cytokine signaling (Auffray 2009; Danilin 2012). Monocytes are comprised of discrete functional subsets such as MDSCs, which are typically tumor-associated and identified in mice as mononuclear Gr1⁺CD11b⁺. MDSC proliferate in the spleen in response to tumor progression and impair regulatory T cell activity (Auffray 2009). Therefore, we hypothesize that circulating mononuclear cells are effective biologically active carriers of cancer nanotherapeutics. To test this hypothesis, a mixed population of mononuclear immune cells were harvested from the spleens of immunocompetent PyMT mice and examined for their

potential to deliver cargo to endogenous mammary epithelial tumors and compared to fully mature macrophages derived from bone marrow.

3.2 METHODS

3.2.1 Establishment of PyMT Mice

All procedures involving mice were conducted in accordance with the National Institutes of Health regulations concerning the use and care of experimental animals. This study was approved by the University of New Mexico School of Medicine Institutional Animal Care and Use Committee.

Immune cell mediated targeted drug delivery studies require animal models with an intact immune system. The MMTV-PyMT mouse model used in this study is immunocompetent and spontaneously develops mammary epithelial tumors that mimic tumor progression in human breast cancer (Fluck 2009).

FVB/N-Tg(MMTV-PyVT)634Mul/J (MMTV-PyMT) mice were purchased from the Jackson Laboratory (Bar Harbor, ME) and housed in the animal research facility at the University of New Mexico School of Medicine. The mice were maintained at 22-23°C on a 12 hour light and dark cycle and their genomic DNA assessed through polymerase chain reaction around 5 weeks of age to assure the PyMT genotype. PyMT mice developed epithelial carcinomas over the course of 10-12 weeks prior to testing.

3.2.2 Extraction of Mononuclear Immune Cells from Spleen

TAM progenitor cells have been shown to continuously seed tumors by renewing TAM subsets. These myeloid progenitor cells produce a tumor-

monocyte pool of Ly6C high expressing circulating mononuclear cells (Movahedi 2010). Though in clinical applications these cells can be enriched from blood, the blood volume of mice is insufficient for extracting mononuclear cells. Therefore, circulating mononuclear cells were harvested from the spleen reservoir of female PyMT mice by maceration of the spleen using the rubber stopper of a 10 mL sterile syringe over a 40-micron sterile strainer connected to a 50 mL conical vial. The strainer was rinsed with 10 mL Roswell Park Memorial Institute Medium (RPMI-1640) media (HyClone) and the cells pelleted by centrifugation at 400 x g for 10 min. at room temperature and resuspended in RPMI-1640 medium for purification of mononuclear cells (Kruisbeek 2001).

3.2.3 Purification of Mononuclear Splenocytes

Mononuclear splenocytes (MS) were density gradient separated from the spleen via flotation. Four volumes of 60% (w/v) OptiPrep (Sigma Aldrich) were mixed with two volumes of RPMI-1640 to produce a solution of density 1.215 g/mL. Splenocytes were suspended in 3.9 mL of media and gently mixed with 2.1 mL of the 1.215 g/mL density gradient. One milliliter of media was layered on top and the solution was centrifuged at 1500 x g for 20 min at 4°C in a swinging bucket rotor (Fisher 1998). MS were extracted from the floating layer of the density gradient (Figure 1 A, red arrow) and washed two times with RPMI-1640 to remove residual density gradient medium. Viability post density gradient isolation was assessed by flow cytometry using Live/Dead Violet Dead Cell Stain Kit (Life Technologies). In summary, the cell suspension was adjusted to 1×10^6 cells/mL in 1X phosphate buffered saline (PBS). Live/Dead violet dye was

added to the solution at a 1% concentration and incubated on ice for 30 min. Following staining, the cells were washed several times by centrifugation at 500 x g for 10 min. and resuspended in 1X PBS. Finally, the cells were fixed in 4% paraformaldehyde (PFA) for 15 min. and analyzed by flow cytometry.

3.2.4 Preparation of Bone Marrow Derived Macrophages (BMDM)

Bone marrow was harvested from 10 week old female PyMT mice and the femurs and tibias extracted and placed in a dish of 70% ethanol prior to extraction of the bone marrow. Bone marrow was flushed out of the bones onto a 40 µm cell strainer using a 10 mL syringe with a 27 gauge needle. The bone marrow was broken apart over the 40 µm strainer using the rubber stopper of a 10 mL syringe and rinsed with serum free Dulbecco's Modified Eagle's Medium (DMEM) media into a 15 mL conical vial. The subsequent strained cells were pelleted by centrifugation at 500 x g for 5 min. and resuspended in L-cell conditioned media. The bone marrow cells were then conditioned towards M1 phenotype in culture with L-cell conditioned media for seven days at 37°C and 5% CO₂. L-cell media was refreshed on the fourth and sixth day of conditioning. Differentiated BMDM were then characterized as described below.

3.2.5 Morphological Analysis of MS and BMDM

Cell morphology was characterized *in vitro* by May-Grünwald-Geimsa staining. Cells were smeared onto SuperFrost Plus microscope slides and allowed to air dry after fixation with 4% PFA at room temperature or 100% methanol fixation on ice for 15 min. The cells were then stained with 0.2% May-Grünwald's eosin-methylene blue in methanol for 5 min., followed by staining

with Geimsa working solution (73% methanol, 26% glycerol, 0.6% Geimsa's Azur-Eosin-Methylene Blue) for 12 min. The slides were then washed with clean 67 mM potassium dihydrogen phosphate buffer for 2, 5, and 2 min. The slides were allowed to air dry prior to mounting with Permount. Finally, the stained cells were imaged in a Nikon microscope at 100X with oil immersion.

3.2.6 Phenotypic Analysis of MS and BMDM

The purified MS and BMDM were surveyed for particular cell surface expression of an adhesion G protein-coupled receptor called F4/80, which is associated with mature M1 macrophages. The MS and BMDM populations were also surveyed for receptors indicative of myeloid derived suppressor cells, such as the myeloid differentiation antigen (Ly6C/G (GR1)) and integrin receptor CD11b. Quantitative analysis regarding purity and percent viability of enriched MS and BMDM was assessed by flow cytometry and fluorescence microscopy. Enriched MS and BMDM were immunostained by first blocking Fc receptors with 5 ug/mL anti-mouse CD16/32 antibody (BioLegend) for 10 min. at room temperature. The cells were then stained with 0.5 ug/mL FITC anti-mouse CD11b or F4/80 and PE anti-mouse Ly6C/G (Gr1) antibodies (BioLegend) for 20 min. on ice and washed twice by centrifugation at 400 x g for 10 min. and resuspended in Hanks Balanced Salt Solution (HBSS) with 0.5% horse serum (Movahedi 2010). Finally, the cells were stained with 1% Live/Dead Violet for 30 min. on ice and washed twice as described in section 3.2.3. The cells were fixed in 4% PFA for 15 min. at room temperature, washed twice in 1X PBS and resuspended to a concentration of 1×10^6 cells/mL in 1X PBS for flow analysis

using a BD Fortessa four color flow cytometer. Size and granularity were gated on the unstained sample. Antibody specificity was confirmed with PE and FITC isotype controls (BioLegend). Compensation of fluorochrome emission overlap was assessed using single FITC, PE, and Violet controls.

3.2.7 Phagocytic Capacity of MS and BMDM

To establish the proportion of phagocytic MS harvested from the spleen, the cells were labeled by phagocytosis of PKH26 dye aggregates (Sigma Aldrich). PKH26 forms dye micro-aggregates that are resistant to metabolic attack, thus remaining intact within cells post ingestion. Isolated monocytes were resuspended in 1 mL of Diluent B for precipitation of PKH 26 into 100 nm micelles and incubated with 10 μ m PKH26 Red Fluorescent Cell Linker for 5 min. at room temperature. Following the incubation, 2 mL of horse serum was added to quench the reaction and the cells were washed twice in Dulbecco's PBS with 0.5% horse serum or RPMI-1640 media. The cells were then fixed with 4% PFA for 15 min. and analyzed by flow cytometry. Size and granularity were gated on the unstained sample. Quantitation of PKH26 positive cells was calculated proportional to 10,000 events.

M1 macrophages have a unique ability to ingest large particles that are not identified as part of the host. To confirm this ability in the simulated M1 macrophage population, BMDM were incubated with 1 μ m yellow-green fluorescing latex beads (Sigma Aldrich) for one hour at 37°C and 5% CO₂. The BMDM were washed several times with DMEM to remove the excess beads and stained using May-Grünwald-Geimsa staining or Rhodamine-phalloidin staining

of actin and 4',6-Diamidino-2-phenylindole, dilactate (DAPI) staining of the nucleus for fluorescence microscopy.

3.3 RESULTS

3.3.1 Viability and Morphology of MS and BMDM

Figure 1 A (red arrow) shows the population of MS enriched by density gradient separation (described in Section 3.2.3). Flow cytometric analysis of MS viability post isolation suggests that the majority of MS survive density gradient enrichment, though ~18% of the population showed signs of cell death (Figure 1B). In Figure 2 A, May-Grünwald-Geimsa staining of the density gradient separated flotation layer of PyMT splenocytes shows predominantly mononuclear morphology. The variable nuclei morphologies and cytoplasm to nucleus ratios of the MS, shown in Figure 2 A, are typical of mixed monocyte populations (Sliwkowski 2013). *In vivo* biodistribution studies (see Chapters 4 and 5) MS are compared against fully differentiated M1 macrophages to determine if the maturity of mononuclear immune cells affected targeted delivery to mammary epithelial tumors. Here, May-Grünwald-Geimsa staining shows that the BMDM were significantly larger and more oblong in shape, suggesting the population is largely composed of cells exhibiting the macrophage phenotype (Figure 2B).

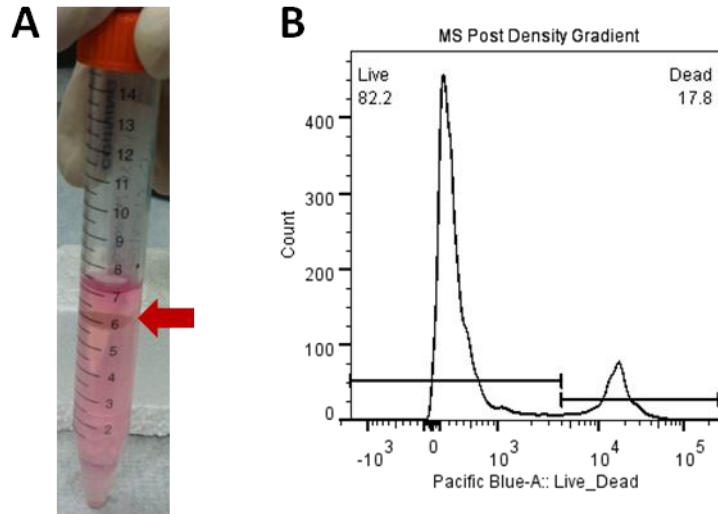


Figure 1: Density Gradient Isolation of Mononuclear Splenocytes (MS). The MS cell layer after density gradient separation (A, red arrow) is captured between the top layer of Optiprep and the bottom layer of RPMI-1640 medium after centrifugation. Density gradient separated MS were stained with Live/Dead Violet and analyzed by flow cytometry to confirm that the majority of the mononuclear cell population (82.2%) remain viable post density gradient separation (B).

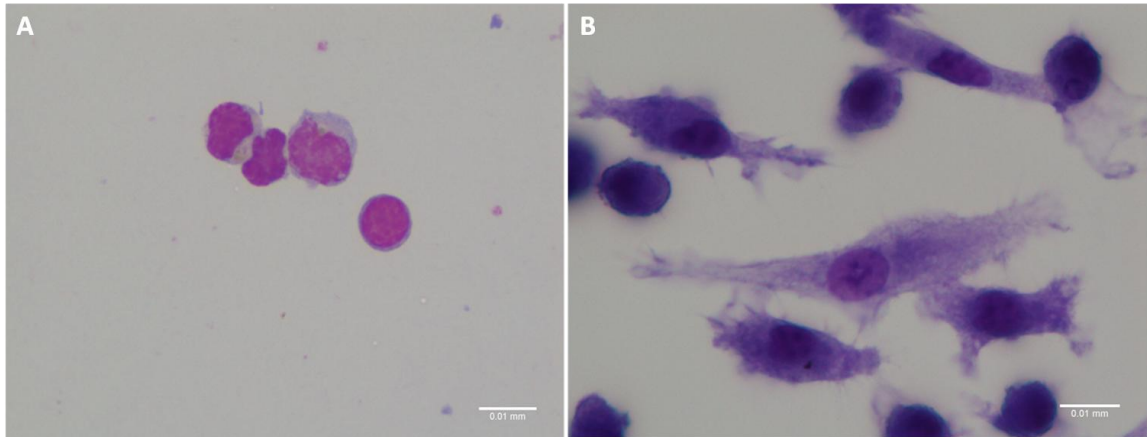


Figure 2: Morphology of Density Gradient Separated Mononuclear Splenocytes (MS) and Bone Marrow-Derived Macrophages (BMDM). May-Grünwald-Geimsa stained MS exhibited predominantly lymphocyte morphology with a prominent circular nucleus and high nucleus-to-cytoplasm ratio (A). BMDM, cultured in L-cell conditioned media for 7 days, are significantly larger and more spread out with a much smaller and more uniform cytoplasm-to-nucleus ratio (B). Both images taken at 100X under oil immersion and the scale bar measure 0.01 mm.

3.3.2 Phenotype of MS and BMDM

TAMs are generally defined as CD11b⁺ F4/80⁺ and can adopt further subphenotypes depending on the tumor microenvironment, such as becoming classically activated (M1) or immunosuppressive (M2) macrophages (Chioda 2011). In order to assess whether TAMs or immature myeloid cells are more effective tumor targeting immune cells post IV injection, density gradient purified MS were compared against BMDM. Flow cytometry demonstrated that BMDM exhibited higher expression levels of F4/80 (Figure 3B), whereas only a small subset of the MS population stained positive for F4/80 (Figure 3D). BMDM were predominantly CD11b positive (91%), whereas the MS population expressed very low levels of CD11b and higher levels of Ly6C (~13%) (Figure 3 A&C).

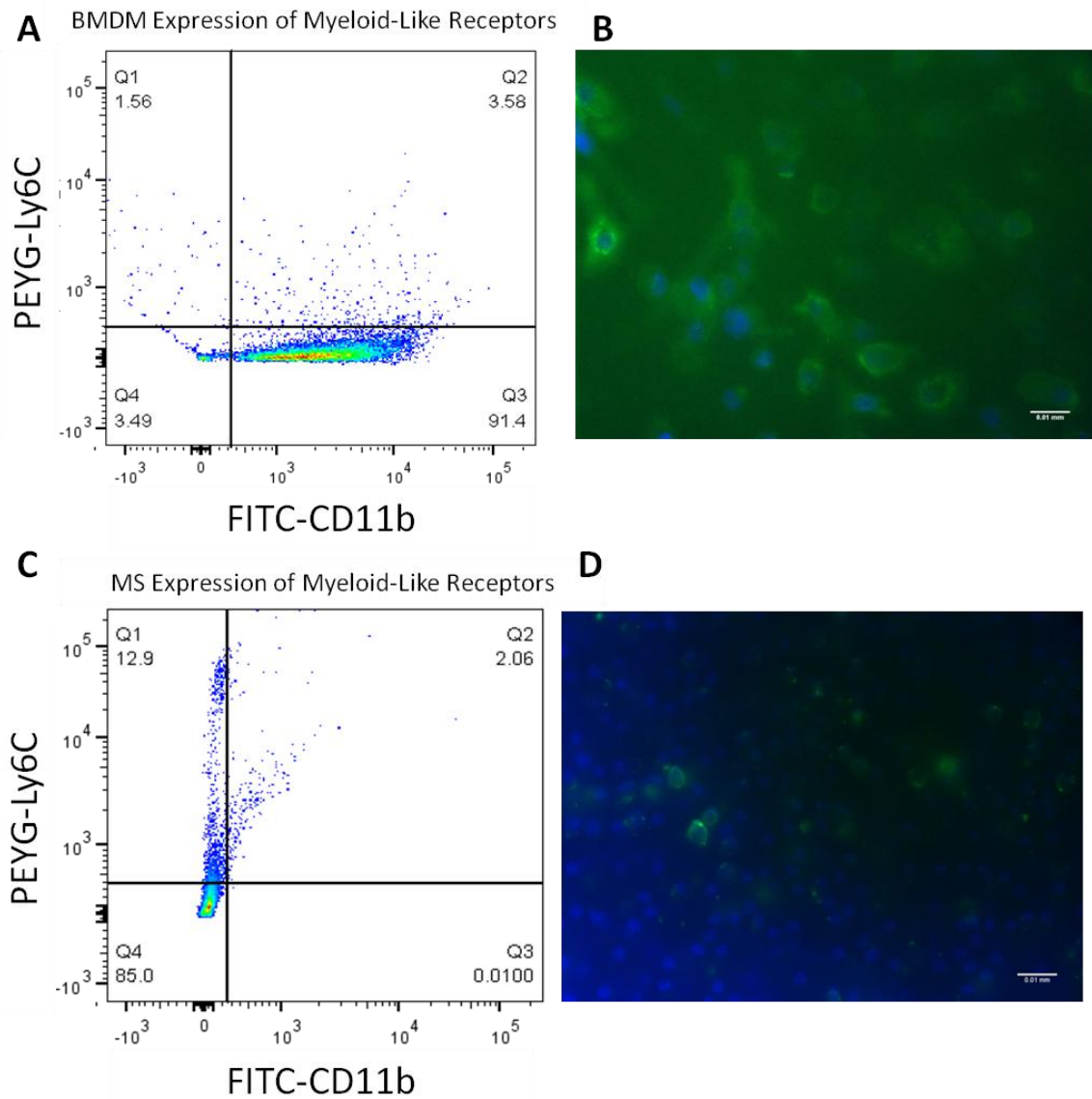


Figure 3: MS and BMDM Expression of Myeloid-like Receptors. Flow cytometry of BMDM confirms CD11b expression with minimal Gr1 expression (A). Fluorescence microscopy at 32X of BMDM confirms predominant F4/80 expression (green with the nuclei counterstained blue using DAPI), which is characteristic of M1 macrophages (B). Fluorescence microscopy (32X) of MS shows that only a small fraction express F4/80 (green with blue DAPI stained nuclei). Flow cytometry of MS demonstrates a predominance of Ly6C expressing cells (C). The scale bars measures 0.01mm.

3.3.3 Phagocytic Capacity of MS and BMDM

Fluorescence microscopy of MS incubated with 100 nm PKH26 micelles (red) shows a subset of MS took up PKH26 (Figure 4A, gate P2). Flow cytometric

analysis of MS incubated with PKH26 micelles shows that the 35.5% of the MS population identified as monocyte/macrophage lineage (by forward scatter/side scatter) exhibit a high level of PKH26 micelle uptake (Figure 4A, gate P1) with 99% of this subpopulation identified as strongly PKH26 positive (Figure 4B, left). By contrast the remaining MS population was 71.8% positive for PKH26 staining (Figure 4A, gate P2), but the fluorescence intensity was more than an order of magnitude lower than the fluorescence intensity of the monocyte/macrophage sub-population (Figure 4B, right), suggesting the monocyte/macrophage subpopulation has a higher cargo loading capacity. This shift in fluorescence intensity is consistent with the distribution of PKH26 loaded MS shown by fluorescence microscopy (Figure 4C).

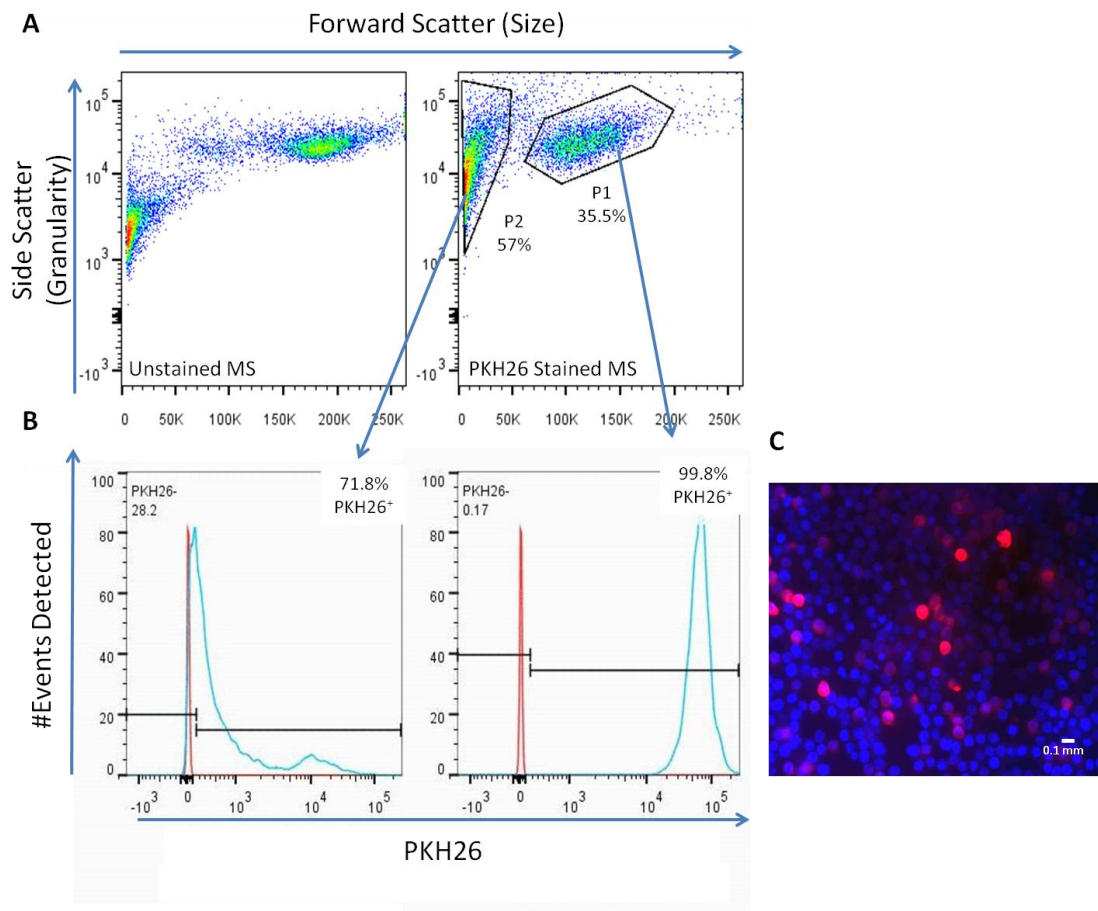


Figure 4: MS Phagocytosis of PKH26 Cytotracker. Flow cytometric analysis of MS uptake of 100 nm PKH26 micelles compared to unstained MS show the MS do not autofluoresce in the PE channel, which excites PKH26 dye (red). About 35% of the MS population exhibited forward and side scatter characteristics of monocytes and macrophages (A, P1) and 99% of the gated monocyte/macrophage population stained positively for PKH26 (B right). The majority of the remaining cell population (~72%) also stained for PKH26 (A, P2) with an overall lower intensity (B left). The proportion of PKH26 loaded MS is visualized at 20X via fluorescence microscopy (C). The nuclei are stained with DAPI (blue) and the PKH26 micelles are shown in red (scale bar measured 0.1 mm).

M1 macrophages have a unique ability to ingest large particles that are not identified as part of the host. Therefore, BMDM were incubated with yellow-green fluorescent latex beads to confirm that the BMDM are phagocytic. Both

May-Grünwald-Geimsa staining and fluorescence analysis confirm the M1 phagocytic phenotype (Figure 5).

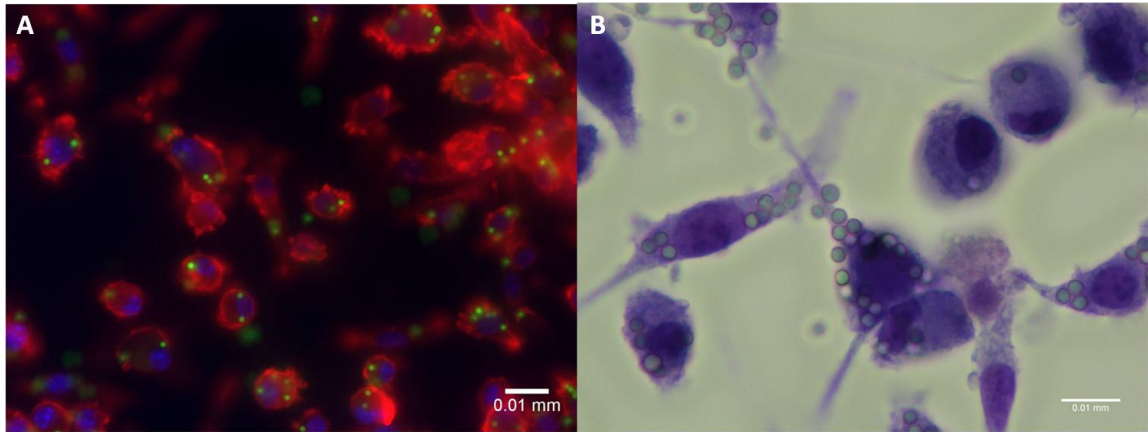


Figure 5: BMDM phagocytosis of 1 µm latex beads. The phagocytic phenotype of BMDM was confirmed by co-incubation with 1 µm yellow-green latex beads. The BMDM actin cytoskeleton was stained with Rhodamine phalloidin (red) and the nucleus stained with DAPI (blue) and imaged at 32X to help determine if the latex beads were phagocytosed by the BMDM (A) Phagocytosis was confirmed by May-Grünwald-Geimsa staining at 100 X, 0.01 mm scale bar (B).

Chapter 4

In Vivo Biodistribution of MS and BMDM

4.1 INTRODUCTION

In the previous Chapter, we demonstrated isolation and characterization of viable MS and BMDM populations and confirmed their ability to phagocytose nano or microparticle cargo. Thus, these cell populations display many of the necessary characteristics to be effective at transporting a drug cargo into tumors *in vivo*. In order to further demonstrate that one or both of these cell populations is suitable for drug delivery, the *in vivo* biodistribution of these cell populations were assessed after adoptive transfer, a process which involves harvesting the cells from a donor mouse, labeling the cells *in vitro*, and injecting the labeled cells into a recipient mouse.

4.2 METHODS

4.2.1 SPECT/CT Imaging of MS and BMDM Biodistribution

To test the principle of immune cell mediated tumor targeting, mononuclear splenocyte migration was tracked *in vivo* post IV injection and compared against BMDM biodistribution, in both tumor (PyMT) and non-tumor bearing (FVB) mice. MS and BMDM were prepared as described in Sections 3.2.2, 3.2.3, and 3.2.4. The cells were then labeled by a lipid-soluble metal complex of gamma emitting Indium-111 with tropolone for detection by SPECT/CT (Dewanjee 1981). Metal chelation of Indium-111 to tropolone was facilitated by adding 0.36 mL of tropolone to 0.48 mL of indium chloride and the pH adjusted to 7.0-7.5 with 0.1

M sodium hydroxide. The indium was incubated with tropolone for 15 min. at room temperature, after which MS or BMDM were resuspended in serum free RPMI-1640 media and incubated with 0.9 mL of the indium-tropolone solution at 37°C for 45 min. while rocking. The cells were then pelleted by centrifugation at 200 x g for 5 min. and resuspended in 2.4 mL media and maintained at 37°C for IV injection.

One hundred microliters of indium labeled MS were adoptively transferred into four 10 week old female FVB and PyMT mice at a concentration of 3×10^6 cells/100 μ L. The same volume of indium labeled BMDM were adoptively transferred at 200,000 cells/100 μ L into one 10 week old female FVB and one 10 week old female PyMT mouse, due to insufficient quantity of BMDM cultured from bone marrow. All mice were imaged at 30 min., 5 hrs., and 24 hrs. post injection using Single-Photon Emission Computed Tomography (SPECT) and Computed Tomography (CT) (NanoSPECT/CT[®] Small Animal In Vivo Imager, Bioscan, Inc., Washington, D.C.). The mice were dosed intravenously via lateral tail vein injection with approximately 500 μ Ci of Indium-111 and anesthetized at 30 min., 5 and 24 hrs. post injection using Isoflurane in an anesthesia induction chamber at 3% (with 2.5% LPM oxygen) and then placed on a heated bed (37°C) in the imaging system. A topogram was done to determine the scan range needed for the CT and SPECT acquisitions. Topogram acquisition parameters consisted of 65 kVp tube voltage, 500 ms exposure time, and all mice were prone in a feet first position. Once the scan range was determined, the 3 min. CT acquisition was completed using 180 projections with a pitch of 1.5. Helical

SPECT options included 32 projections and varying time per projection for estimated acquisition times of about 24 min. Mice remained anesthetized at 2% isoflurane (with 2.5% LPM Oxygen) during the entire imaging process and were sacrificed post imaging.

4.2.2 Quantitative Analysis of SPECT/CT Image Data

The helical SPECT/CT images were reconstructed and regions of interest (ROIs) selected for quantitative analysis of MS biodistribution using VivoQuant 1.22 software (inviCRO, LLC). For both PyMT and FVB mice, ROIs of central axial sections were selected within mammary tumors or normal mammary glands (ROIs within right mammary and left mammary at level 1, and a single ROI covering both right and left mammary tissue at level 5); central axial sections of liver, left kidney, and spleen were also selected. The mean and standard deviation of the Indium-111 SPECT signal were computed for all ROIs and the data were plotted and analyzed using Prism statistical software. Mammary signal was plotted as a function of incubation time and the data were fit using linear regression, where the significance of the difference in slope and elevation were assessed.

4.2.3 Activation of MS versus Incubation Time at 37°C

MS were prepared as described in Section 3.2.2 and 3.2.3 and then treated to mimic the injectate sample conditions from the previously described SPECT study in Section 4.2.1. Specifically, MS were incubated in RPMI at 37°C for 30 min, 2 hrs., and 4 hrs. in a sealed container (without CO₂ buffering). Activation was assessed using a mouse monocyte cytokine array panel (R&D systems).

Briefly, cell culture supernatant was exposed to nitrocellulose membranes, previously blocked with serum, spotted with GM-CSF, IFN γ , IL-1 β , IL-2, IL-4, IL-6, IL-10, IL-13, MCSF, and TNF α antibodies overnight. The membranes were then washed in buffer several times before incubation with biotinylated IR Dye 800 CW for 1 hr. The membranes were again washed several times with buffer and the fluorescently labeled captured antibodies imaged on a LiCor scanner. The total fluorescence was background corrected and calculated by multiplying the mean fluorescence of background to the area of the selected region of interest, which was then subtracted from the integrated density calculated in ImageJ (National Institutes of Health). As a positive control, RAW 264.7 immortalized murine macrophages were stimulated with 100 nM lipopolysaccharide from *E. coli* for 1 hr at 37°C to induce cytokine expression.

4.2.4 Effect of Incubation at 37°C on MS Phenotype and Phagocytosis

MS were prepared as described in Section 3.2.2 and 3.2.3 and treated to mimic the injectate sample conditions from the previous SPECT study. The MS were incubated at 37°C for 30 min., 2 hrs., and 4 hrs. in a sealed microfuge tube (without CO₂ buffering) prior to immunological staining and labeling by PKH26 micelle phagocytosis (described in Section 3.2.7). MS were immunostained with 0.5 μ g/mL FITC anti-mouse CD11b or F4/80, Brilliant Violet anti-mouse CD11c and PE anti-mouse Ly6C/G (Gr1) antibodies as described in Section 3.2.6. The cells were fixed in 4% PFA for 15 min. at room temperature, washed twice in 1X PBS and resuspended to a concentration of 1×10^6 cells/mL in 1X PBS for flow analysis using a BD Fortessa four color flow cytometer. Size and granularity

were gated on the unstained sample. Antibody specificity was confirmed with Brilliant Violet, PE and FITC isotype controls (BioLegend). Compensation of fluorochrome emission overlap was assessed using single FITC, PE, and Violet controls.

4.2.5 Demonstrating Tumor Infiltration of Cargo-Loaded MS

To obtain visual confirmation of MS biodistribution in tumor bearing PyMT mice, and to investigate distribution at longer time points, 2×10^6 PKH26 loaded MS were adoptively transferred into eight 10-12 week old PyMT mice and allowed to circulate for 5 hrs., 24 hrs., 48 hrs., or 72 hrs. (N=2 per time point). Each mouse was sacrificed at the appropriate time point, and the tumors were cryopreserved by immersion in Optimal Cutting Temperature (OCT) (VWR) followed by snap freezing in liquid nitrogen. The tumors were then sectioned into 5 μ m slices onto SuperFrost Plus microscope slides using a freezing microtome and fixed in 4% PFA for 15 min. at room temperature. The sections were then stained with Hematoxylin and eosin, mounted in Permount (Fisher) and imaged on a Nikon microscope at 20 and 100X. A subset of both *in vitro* and *in vivo* sections were also stained with 5 μ g/mL wheat germ agglutinin (Invitrogen) for 10 min. at room temperature, washed twice with 1X PBS and mounted in Vectashield with DAPI for fluorescence image analysis and a Zeiss M200 microscope at 20X and 32X.

4.2.6 Purification of Myeloid-Derived Stem Cells from MS

The Ly6C(Gr1)/CD11b double-positive cells were enriched using mouse monocyte enrichment kits (StemCell). MS were incubated in EasySep selection

cocktail for 15 min prior to incubation with selective magnetic nanoparticles for 10 min. CD11b⁺ cells were enriched by negative selection and Ly6C⁺ cells were positively selected by magnetic separation using two StemCell enrichment kits.

4.3 RESULTS

4.3.1 SPECT/CT Imaging of MS and BMDM Biodistribution

Qualitatively, the SPECT/CT images of radiolabeled MS suggest a patterned migration that changes over the course of 24 hrs. Within 30 min. post-adoptive transfer, the majority of the radiolabeled MS were detected on tomographic images within the liver, spleen, and kidneys of both PyMT and FVB mice, with some signal in the heart and chest area (Figure 6, green arrow). By 5 hrs., in both PyMT and FVB mice, the majority of the MS had migrated to the liver, kidneys and spleen (Figure 7). The biodistribution of MS in PyMT versus FVB diverged after 5 hrs. In half of the PyMT cohort, MS were visible in the mammary epithelial tumors of PyMT mice, relative to the surrounding tissue, while, visually, no signal was observed in the normal mammary glands of corresponding FVB mice (Figure 7, red arrows). MS migration to tumors appeared to be more prevalent in larger tumors. There was consistent signal in the joints (e.g. knees and shoulders) of FVB mice that did not correspond in PyMT mice (Figure 7, green arrow). By 24 hrs., MS delivery to mammary epithelial tumors further increased in PyMT mice, while no signal was visually apparent in the mammary glands of FVB mice, even after 24 hrs. However, MS

presence appeared to further increase in the joints of FVB mice after 24 hrs. circulation (Figure 8).

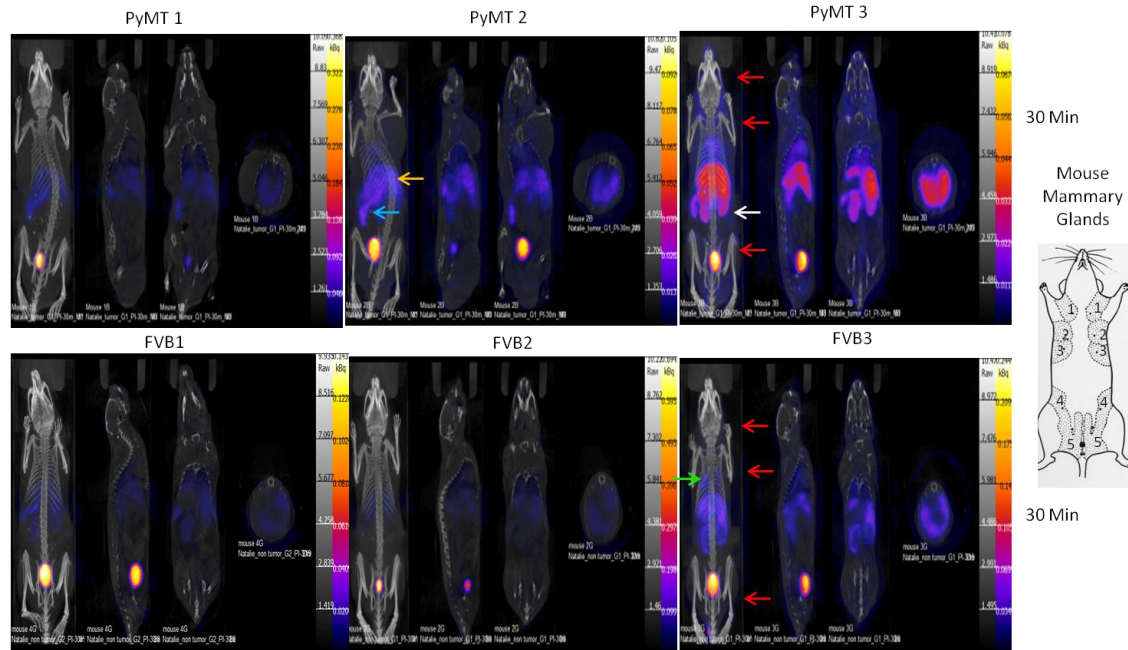


Figure 6: Biodistribution of Radiolabeled MS in PyMT and FVB Mice after 30 min. Circulation. SPECT/CT was used to follow the migration of Indium-111 labeled MS, post adoptive transfer, in PyMT (tumor bearing) and FVB (non-tumor bearing) mice at 3 time points over 24 hrs. At 30 min., SPECT images suggest the majority of adoptively transferred MS migrate to the chest (green arrow), liver (yellow arrow), spleen (blue arrow), and kidneys (white arrow) of PyMT and FVB mice.

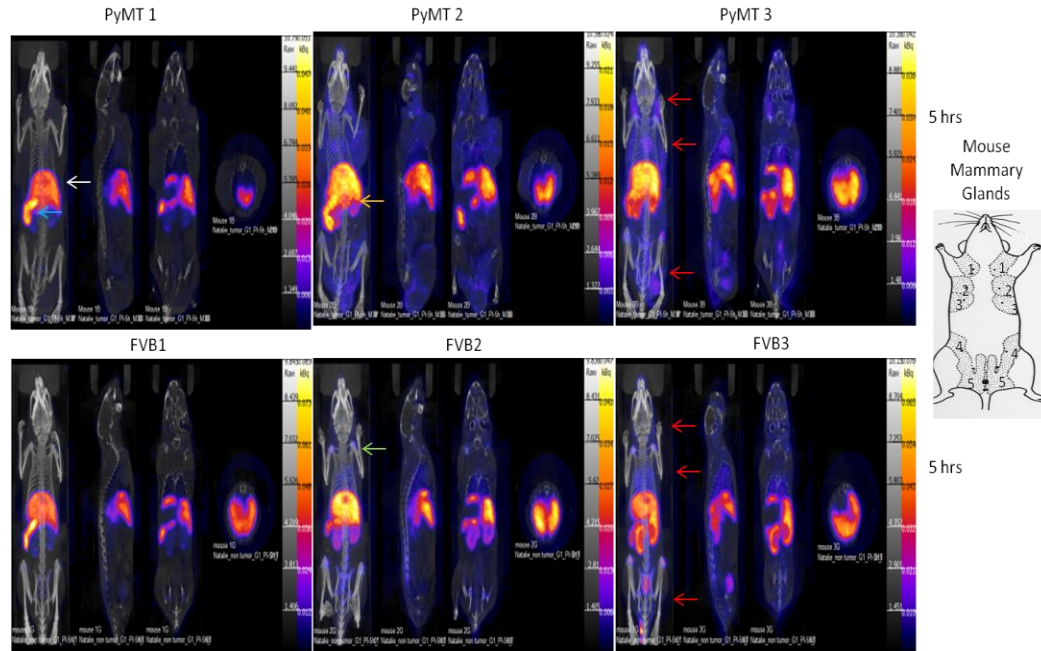


Figure 7: Biodistribution of Radiolabeled MS in PyMT and FVB Mice after 5 hrs. Circulation. SPECT/CT was used to follow the migration of Indium-111 labeled MS, post adoptive transfer, in PyMT (tumor bearing) and FVB (non-tumor bearing) mice at 3 time points over 24 hrs. After 5 hrs. circulation post adoptive transfer, the MS have migrated out of the chest area and begin to appear in tumors (red arrows), though not in the mammary glands of FVB mice (red arrows). There is also some migration to the joints (green arrow) in FVB mice after 5 hrs.

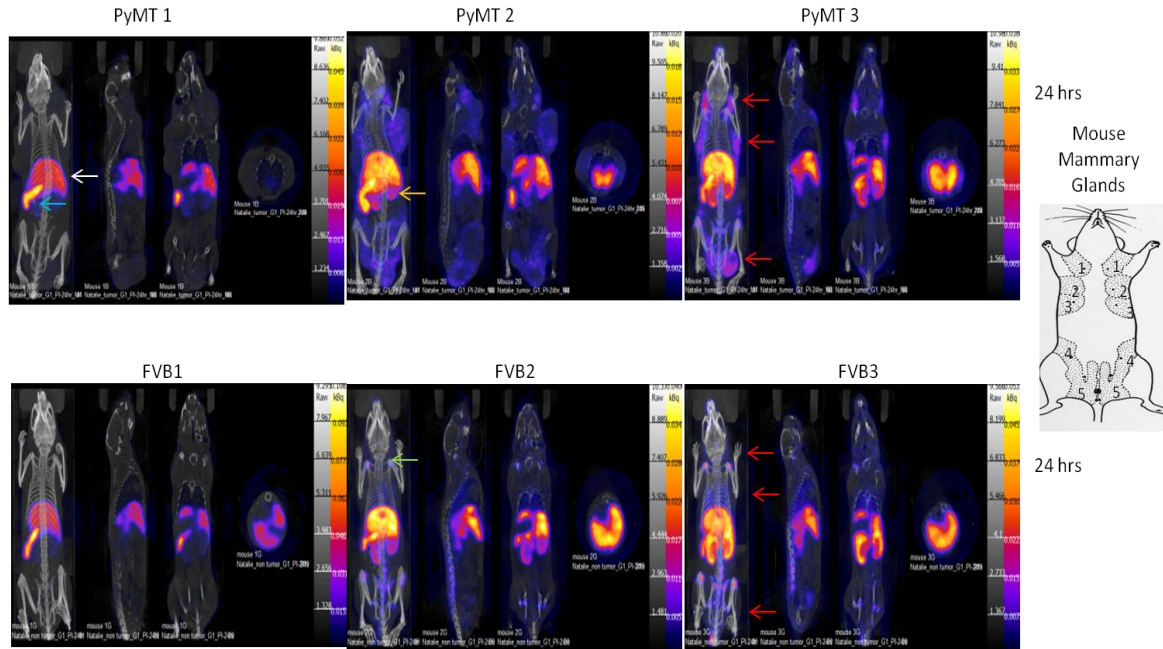


Figure 8: Biodistribution of Radiolabeled MS in PyMT and FVB Mice after 24 hrs. Circulation. SPECT/CT was used to follow the migration of Indium-111 labeled MS, post adoptive transfer, in PyMT (tumor bearing) and FVB (non-tumor bearing) mice at 3 time points over 24 hrs. SPECT images suggest the MS tumor signal is increased after 24 hrs. circulation post adoptive transfer (red arrows), though not in the mammary glands of FVB mice (red arrows).

Quantitative analysis of three PyMT and three FVB mice injected on the same day reveals an interesting time dependence of the mammary signal on the injection time (Figure 9A). The MS injectate was radiolabeled at the same time, but the injections of the six animals were carried out over the course of the day, such that the pairs of mice (one PyMT and one FVB) were injected at approximately 30 min., 2, and 4 hrs. after radiolabeling. The average mammary ROI signals at 24 hrs. post-injection demonstrated a marked increase that is linear in the delay between radiolabeling and injection (Figure 9A). The slopes of the two lines (PyMT and FVB) are significantly different ($p = 0.005$) with a much greater increase in mammary uptake versus incubation time (i.e. greater slope) observed for the tumor-bearing cohort. The affinity of radiolabeled MS for

tumors versus normal mammary tissue was 3.5-fold greater regardless of the incubation time of the sample prior to injection (Figure 9B). Average tumor-to-organ ratios for PyMT and FVB mice are plotted in Figure 9C. The tumor-to-liver, tumor-to-kidney and tumor-to-spleen ratios were greater in PyMT mice relative to FVB, although the result was not statistically significant (Figure 9C).

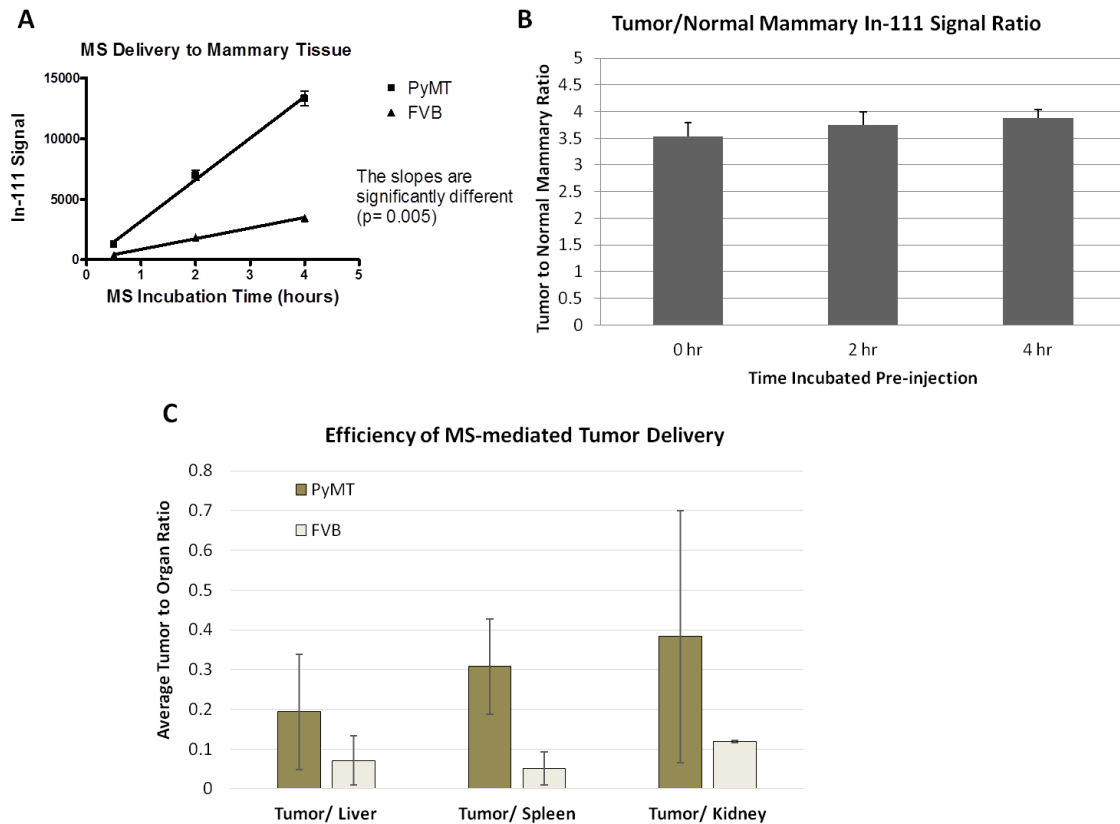


Figure 9: Region of Interest (ROI) Analysis of SPECT/CT images of MS

biodistribution. ROIs of central axial sections were selected for tumors and mammary glands in regions one and five and compared to ROIs of the liver, left kidney, and spleen in PyMT and FVB mice. The mean and standard deviation of the Indium-111 SPECT signal was calculated for all tissues using reconstructed helical SPECT images. The quantified mammary ROI signal suggests a marked increase in tumor association after 24 hrs. that is dependent on the initial sample conditions pre-injection (A). The affinity of MS for tumors over mammary tissue was 3.5-fold greater regardless of the incubation time of the sample prior to injection (B). Tumor-to-organ ratios suggest a trend toward a higher level of uptake by tumor tissue (relative to the liver, left kidney, and spleen) compared to normal mammary tissue (C).

Qualitatively, the biodistribution of radiolabeled BMDM was noticeably different from the biodistribution of MS, as shown in Figure 8. Tomographic images of radiolabeled BMDM post adoptive transfer showed localization primarily in the lungs after 30 min. of circulation (Figure 10 red arrow). After 5 hrs. circulation, the BMDM had begun to migrate out of the lungs into the liver, kidneys and spleen (Figure 10, white, blue, and yellow arrows). By 24 hrs., the lungs had cleared, and the BMDM localized primarily to the liver and spleen and to some extent the kidneys (Figure 10).

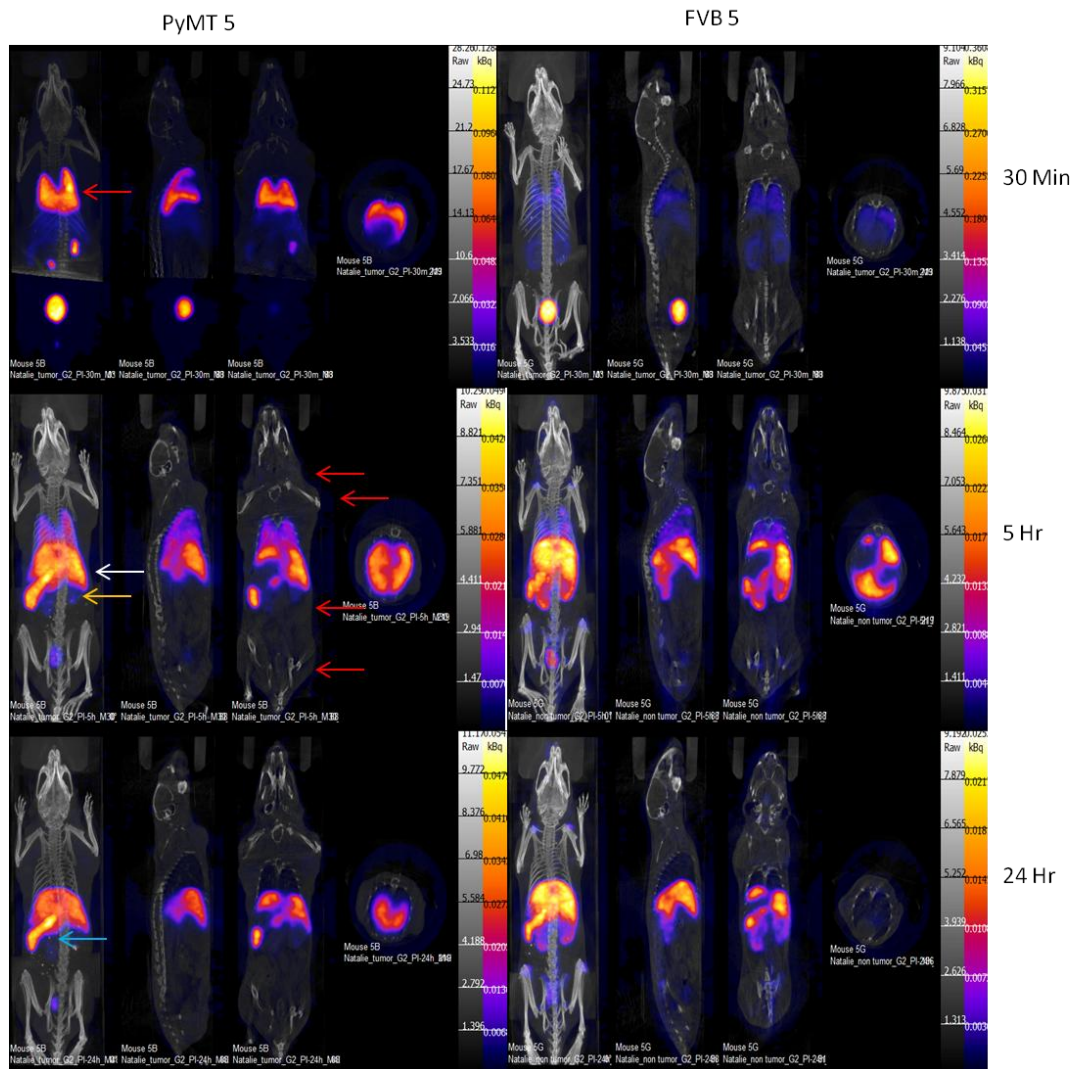


Figure 10: Biodistribution of Radiolabeled BMDM. SPECT/CT imaging was used to track Indium-111 labeled BMDM migration post adoptive transfer in PyMT and FVB mice. SPECT images suggest BMDM primarily migrate to the lungs (pink arrow). Over the course of 24 hrs., the BMDM migrate out of the lungs and into the liver (white arrow), kidneys (yellow arrow) and spleen (blue arrow), but not tumor (red arrows).

4.3.2 Activation of MS versus Incubation Time at 37°C

ROI analysis of SPECT/CT images of MS biodistribution suggest a positive impact of sample incubation time at 37°C prior to injection on the biodistribution of the injectate. The immature nature of the MS makes them particularly susceptible to influence by external stimuli. Therefore, the conditions of the MS

samples used in the SPECT experiment were simulated by harvesting and labeling MS and allowing them to incubated for 30 min., 2 hr, or 4 hr to mimic the conditions the MS experienced prior to injection during the course of the SPECT imaging experiment. Supernatants from three MS samples were collected post purification and PKH26 loading to establish the activation state of the cells after each of three incubation intervals (Figure 11A). RAW 264.7 immortalized macrophages were stimulated with 100 nM lipopolysaccharide from *E. coli* to induce cytokine expression (Figure 11B). The cytokine assay showed only the positive controls excited and, therefore, the MS demonstrated no measureable cytokine expression over the course of up to four hrs. incubation at 37°C without CO₂, (Figure 11A).

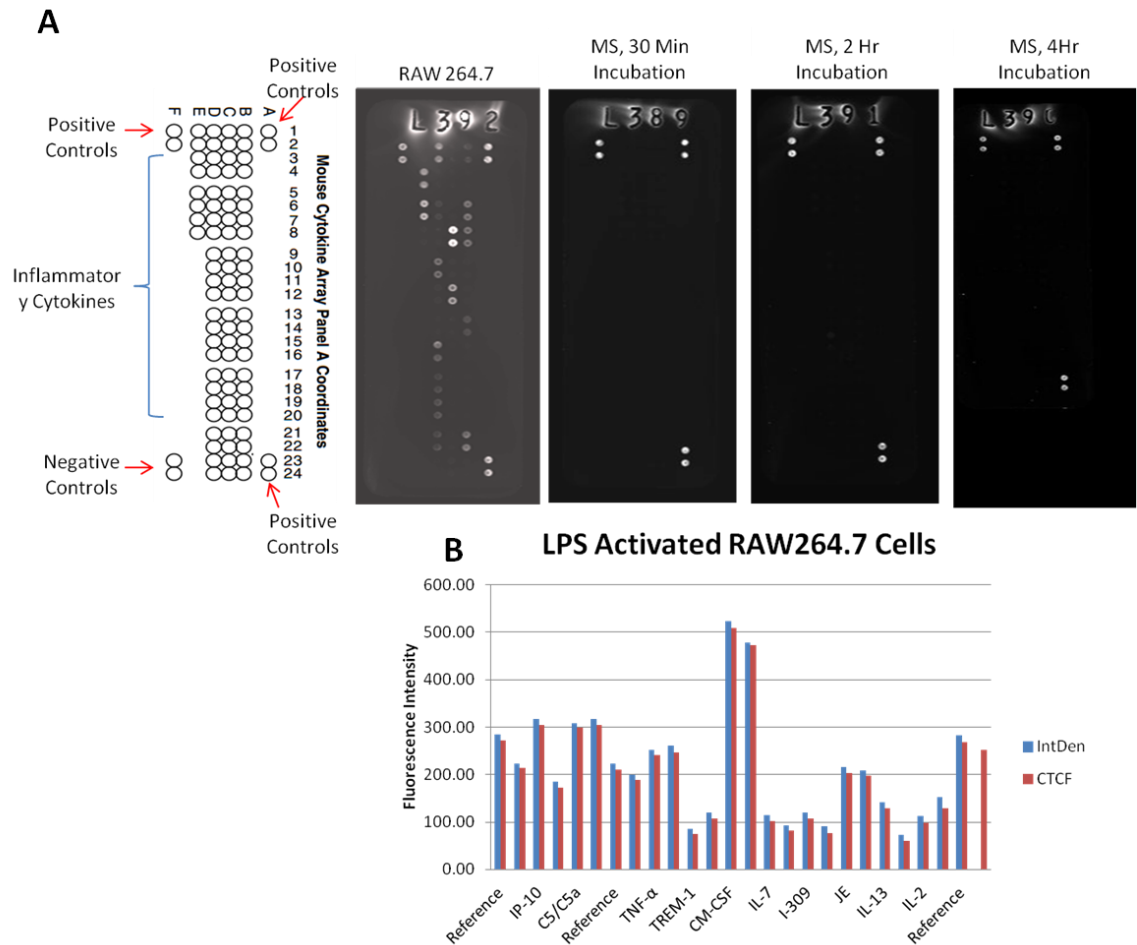


Figure 11: Cytokine array of Pre-injected MS. Density gradient enriched MS were suspended in serum free RPMI-1640 medium for 30 min., 2 hrs., and 4 hrs. at 37°C in sealed vials (without CO₂) to mimic the sample conditions of the MS biodistribution study by SPECT/CT. Cytokine array analysis of the RPMI-1640 supernatants collected after incubation suggest no detectable level of cytokine expression as a function of time incubated at 37°C (A). Immortalized RAW 264.7 mouse macrophages were stimulated with 100 nM LPS to provide a positive control (B).

4.3.3 Effect of Incubation at 37°C on MS Phenotype and Phagocytosis

To further assess the apparent change in Indium-111 labeled MS injectate as a function of incubation time, flow cytometric analysis was performed to quantify potential changes in cell surface expression and the phagocytic capacity of the MS injectate as a function of time incubated at 37°C. However, flow cytometric

analysis showed no appreciable change in cell surface expression of receptors (Figure 12 A&B), although there was a slight increase in PKH26 uptake after 4 hrs (Figure 12C). Shifts in cell size (forward scatter) and granularity (side scatter) suggest a slight divergence of the lymphocyte and monocyte populations and an appearance of a small yet highly granular population after 4 hrs. incubation (Figure 13).

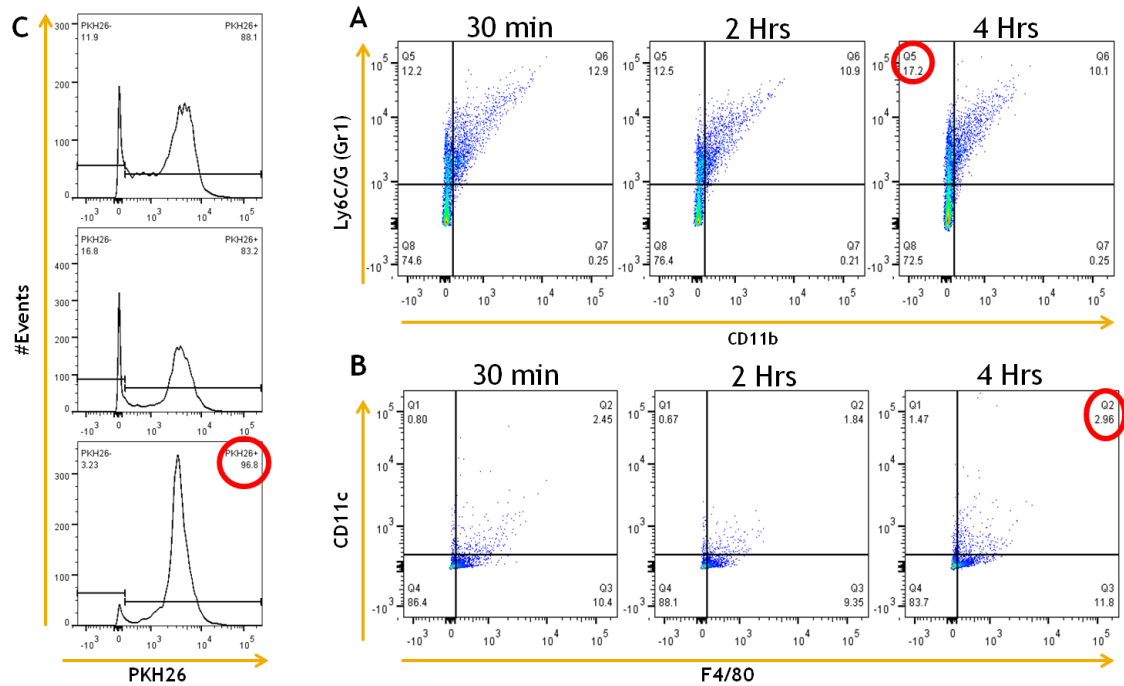


Figure 12: MS Biodistribution Sample Condition Analysis. MS were incubated at 37°C for 30 min., 2 hrs., and 4 hrs. and immunostained with F4/80, CD11b, Ly6C, and CD11c antibodies to elucidate the shift in population dynamics that improved MS biodistribution in vivo. There was no appreciable change in CD11b-Ly6c expression (A) and only a slight change in F4/80-CD11c expression (B). PKH 26 uptake did slightly increase after 4 hrs (C).

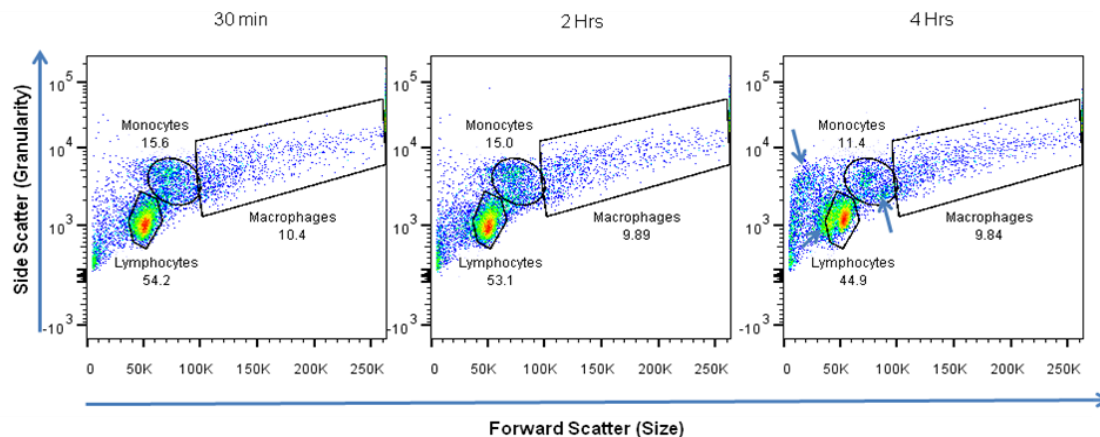


Figure 13: MS Biodistribution Sample Condition Analysis. MS were incubated at 37°C for 30 min., 2 hrs., and 4 hrs. Cell size and granularity were assessed by flow cytometry, which suggests a divergence of the lymphocyte and monocyte populations and an appearance of a small yet highly granular population after 4 hrs. incubation.

4.3.4 Confirmation that Cargo-loaded MS Infiltrate Tumors

In the SPECT study described in Section 4.3.1, the membranes of MS and BMDM were radiolabeled and the cells were not loaded with cargo. To demonstrate that cargo-loaded MS are capable of infiltrating tumors in PyMT mice, and to investigate biodistribution qualitatively at longer time points, 100 nm PKH26-micelle loaded MS were adoptively transferred into PyMT mice and allowed to circulate for 5 hrs., 24 hrs., 48 hrs., or 72 hrs. (N=2 per time point). Representative tumor sections shown in Figure 14 suggest PKH26 dye (red) is localized to branched structures within the tumors that do not appear to stain for DAPI (blue, nuclear stain) (Figure 14 B&C). However, these structures stain strongly with WGA (green), a lectin that stains N-acetyl-D-glucosamine and sialic acid, suggesting a possible extracellular matrix-rich region (Ohno 1986). The micelles are somewhat confined to the WGA-positive structures (Figure 14 F-H). There appears to be a higher quantity of PKH26 micelle localization within the branched structures of the tumor after 5 hrs., which potentially increase over time

(Figure 14 A-D). However, it is difficult to comprehensively assess and directly quantify the PKH26 micelle delivery as a function of time by this method.

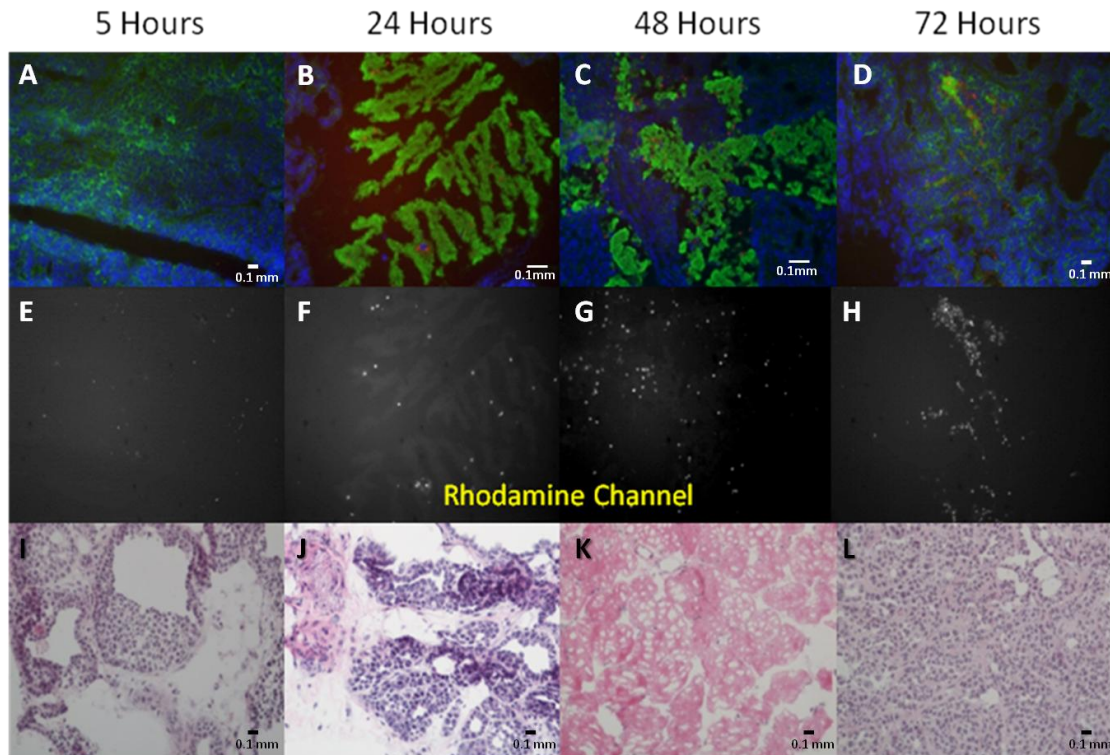


Figure 14: Biodistribution of PKH26 Loaded MS. Fluorescence images of 5 μ m cryosections of a tumor in mammary gland 2/3 were taken at 20X and 32X. The extracellular matrix components were stained with Wheat Germ Agglutinin (green) to elucidate more structure. The nuclei are stained with DAPI (blue). PKH26 fluorescence (red) is observed in the Rhodamine channel (E-H). Images A, D, E, H and I-L were taken at 20X, while images B, C, F, and G were taken at 32X. All scale bars measure 0.1 mm. The corresponding 5 μ m slices of tissue from the similar regions as the fluorescence images were stained with H&E (I-L), though not imaged in the exact same area of the section.

4.3.5 Purification of Myeloid-Derived Stem Cells (MDSC) from MS

In order to determine whether Ly6C(Gr1)/CD11b double-positive MDSC were the subset of the MS population that infiltrated the tumors, we attempted to isolate Ly6C(Gr1)/CD11b double-positive cells, with the intent of using a highly enriched MDSC population in future biodistribution studies. As shown in Figure

15, we demonstrated enrichment of CD11b MS by negative selection and further enrichment of Ly6C(Gr1) positive cells through a positive selection kit, however, the low yield rendered this method impractical for MDSC isolation of sufficient cell quantities required for large *in vivo* biodistribution studies.

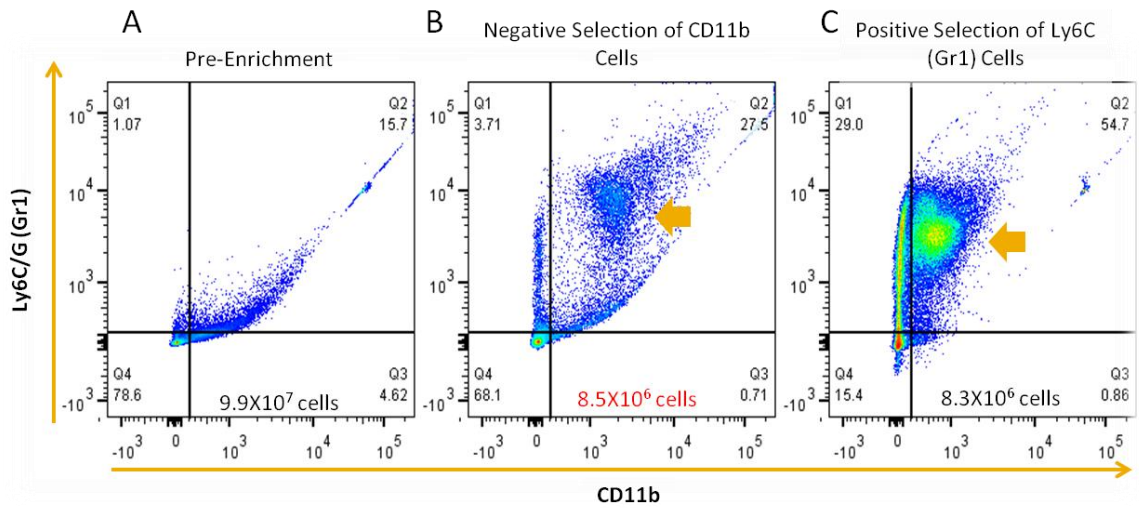


Figure15: Purification of MDSC from the MS population. MS were enriched for cells exhibiting the MDSC phenotype (CD11b+Ly6C+) using a StemCell Negative Selection Kit for CD11b (B) and positive selection kit for Ly6C (C). Although there is significant enrichment of CD11b and Ly6C cells (B&C), there is an appreciable loss of the total number of cells (B in red).

Chapter 5

Characterization and Biodistribution of Protocell-Loaded MS

5.1 INTRODUCTION

Mononuclear phagocytes are currently attractive carrier cells for nanotherapeutics due to their prominent involvement in innate immunity and their capacity to engulf and respond to nanoparticles. As described in the previous chapter, the MS examined in this study demonstrate specific tumor targeting relative to normal mammary tissue, along with the capacity to transport nanoparticles (PKH26 micelles), post-adoptive transfer. Modern cancer therapies are increasingly combining nanotechnology and biotechnology to develop more sophisticated drug formulations and drug release strategies that add to the complexity and behavior of a potential drug cargo. Therefore, it is important to test the compatibility and efficiency of MS-mediated (active) nanoparticle delivery using a more complex cargo. Towards this end, we collaborated with Dr. Eric Carnes and Dr. Carlee Ashley of Sandia National Labs to incorporate protocells, a multi-functional nanoparticle technology, into MS-mediated drug delivery.

5.2 METHODS

5.2.1 Protocell Formulation

Protocells were prepared by liposome fusion to nanoporous spherical silica as described previously (Carroll 2009). Nanoparticle protocells had an overall hydrodynamic diameter of 20-400 nm (180 nm average), which is considered

within the optimal size range to deliver an adequate dose of drugs if distributed homogeneously, such as by IV injection (Ashley 2011; Ashley 2012; Kobayashi 2014). To track the protocells *in vivo*, and to simulate drug encapsulation by the protocells, the nanoporous protocell cores were amine terminated as described previously (Ashley 2011), then reacted with 1 mg DyLight 633 or 650 in ethanol for 8 hrs. at room temperature and washed 3 times in 2X volume of excess 200 proof ethanol prior to liposome fusion.

Initially three liposome formulations were tested in order to optimize MS uptake while avoiding cytotoxicity and MS activation. The various formulations of liposomes were created using previously described methods and fused to the silica nanoparticle cores (Ashley 2011). A synthetic phosphocholine known as 1,2-Dioleoyl-sn-glycero-3-phosphocholine (DOPC) was used as the base lipid, because it commonly forms liposomes in aqueous media alone or in combination with other lipids.

- *DOPC-PEG Protocells.* The first liposome formulation fused to Dylight 633/650 loaded silica spheres was a mixture of DOPC, polyethylene glycol (PEG), and cholesterol at a ratio of 6:1:3, which after fusing to the silica nanoparticle cores results in net neutral surface charged protocells that have a zeta potential of -10 mV in buffer that is near neutral. Previous results have demonstrated IV circulation of DOPC-PEG protocells are typically long-circulating and the PEG functions to shield the particles from MS (Kelly 2011).

- *DOPC-DOTAP Protocells.* The second liposome formulation consisted of a 3:1 ratio of DOPC and N-(1-(2,3-dioleoyloxy)propyl)-N,N,N-trimethylammonium methylsulfate (DOTAP), which is a common liposome transfection agent. The net surface charge of this particle is anionic (-25 mV) which should facilitate rapid non-specific uptake into all cell types along with considerable cytotoxicity.
- *DOPC-DOPS Protocells.* The final liposome formulation was composed of a 1:1 ratio of DOPC and 1,2-Dioleoyl-sn-glycero-3-phosphoserine (DOPS). The DOPC:DOPS particles are positively charged (+25 mV) and employ phosphatidylserines, which are known to be preferentially taken up by macrophages (Kelly 2011).

5.2.2 MS Protocell Uptake and Cytotoxicity Analysis

The concentration of protocells incubated with MS was titrated to optimize protocell uptake while minimizing cytotoxicity to the carrier MS. MS were aliquotted into microfuge tubes at a concentration of 1×10^6 cells/mL and mixed with 0.5, 1, 50, 125, 250, 500, 1000 ug/mL of protocell (DOPC-PEG, DOPC-DOPS, or DOPC-DOTAP) in RPMI-1640 media with 1% horse serum and incubated at 37°C and 5% CO₂ for 20 min., 1 hr and 2 hrs. The cells were then washed by centrifugation at 500 x g for 10 min. and resuspended in serum free media. Viability was assessed by flow cytometry using Live/Dead Violet Dead Cell Stain Kit as described in section 3.2.3. Flow cytometric analysis of the live/dead stained protocells loaded with DyLight 633 and incorporated into MS was gated on live stained and dead stained cells such that the percent protocell

uptake is the proportion of live cells detected that are co-labeled with DyLight 633. All events detected were normalized to 10,000 for comparison between samples.

5.2.3 *In vivo* Comparison of Protocell Loaded MS Biodistribution by Protocell formulation

Density gradient isolated MS were co-incubated at a concentration of 1×10^6 cells/0.1 mL with 125 ug/mL protocells of each protocell formulation (PEG, DOTAP, or DOPS) for 1 hr at 37°C and 5% CO₂. Following incubation, the free protocells were removed from the cell suspension by centrifugation at 500 x g for 10 min. and resuspended in 10 mL 1X PBS. Each category of injectate, pertaining to the particular formulation of protocell cargo, was IV injected into one FVB and two PyMT mice, all 10 weeks old, and circulated *in vivo* for 24 hrs. For comparison, 100 uL of 125 ug/mL protocells were directly injected into 10 week old FVB and PyMT mice and circulated *in vivo* for 24 hrs. The animals were sacrificed after 24 hrs., and the left and right lobes of the liver, the spleen, the kidneys, and all mammary glands or tumors were harvested and divided in half.

One half of each harvested tissue was digested in 62.5 U/mL Hylauronidase, 3 mg/mL Collagenase, and 0.2 µg/mL DNase1 for 3 hrs. at 37°C on a rocker. The digested samples were passed over a 100 µm sterile sieve and washed twice by centrifugation at 500 x g for 10 min. and resuspended in 10 mL RPMI-1640 media. The digested tissue was immediately fixed in 4% PFA for 15 min. at room temperature and washed once in 1X PBS, and subsequently analyzed by flow cytometry.

The second halves of the harvested tissues were fixed whole overnight in 4% PFA and subsequently infused with sucrose prior to immersing in OCT. The OCT embedded tissue was then frozen in isopentane immersed in liquid nitrogen and stored at -80°C for cryosectioning.

5.2.4 SPECT/CT Imaging of DOPC-DOPS Protocell Biodistribution after Direct Injection, MS Adoptive Transfer, and BMDM Adoptive Transfer

Diethylenetriaminepentaacetic acid (DTPA) was amine cross-linked to 50-200 nm nanoporous silica spheres to facilitate DTPA chelation of gamma emitting Indium-111 into protocells for detection by SPECT/CT. The indium was incubated with the DTPA treated nanoporous silica spheres for 30 min. at room temperature in 50 mM Sodium Citrate Buffer. Unbound Indium-111 was removed by centrifugation at 5,000 x g for 4 min. and resuspension in 1 mL of 0.5X PBS. The wash step was repeated one time and the solution spiked with 100 uL of nanoporous silica cores infused with Dylight 650 and the final volume raised to 1.1 mL. An equal volume of DOPC-DOPS liposomes were added to the cores and incubated overnight at 4°C. Prior to loading into MS and BMDM, the excess lipid was removed from the solution by centrifugation at 5,000 x g for 4 min. and resuspension in 1 mL of 1×10^6 cells/0.1 mL of either MS or BMDM in serum free RPMI-1640 media buffered with 20 mM Hank's Balanced Salt Solution (HBSS). The cells were incubated with Indium-111-labeled DOPC-DOPS protocells for 1 hr at 37°C to facilitate protocell uptake and subsequently washed in RPMI-1640 media as described in Section 5.2.2. The cells were

resuspended in 1 mL serum free RPMI-1640 media buffered with 20 mM HBSS and stored on ice prior to injection.

Protocell-loaded MS were adoptively transferred into four 12 week old female FVB mice and four 12 week old PyMT mice at a concentration of 1×10^6 cells/100 μ L. Protocell loaded BMDM were adoptively transferred into four 12 week old female FVB mice. An additional four 12 week old female FVB mice and four 12 week old PyMT mice were directly injected with 630 μ g of radiolabeled protocells mixed with 350 μ g of fluorescent DOPC-DOPS protocells, at a concentration of 10 mg/mL, via IV injection. All mice were imaged by SPECT/CT at 30 min., 5 hrs., and 24 hrs. post injection as described in section 4.2.1. Each animal was sacrificed immediately following the 24 hr imaging time point.

Quantitative analysis of the SPECT/CT images was performed by INVICRO (Boston, MA). ROIs were selected from SPECT/CT images, using volumes corresponding to tumors or normal mammary glands, liver, kidneys, spleen, brain, bone, lungs and heart of all PyMT and FVB mice in the study. The cohorts (BMDM mediated, MS-mediated, and directly injected; PyMT and FVB) were compared against each other, and the mean and standard deviation of the Indium-111 SPECT signal (uptake), expressed as the percentage of the injected dose per gram of tissue (%ID/g), was calculated for all ROIs.

5.3 RESULTS

5.3.1 Optimization of MS Protocell Uptake and Viability

Flow cytometric analysis of MS incubated with various concentrations of three protocell formulations suggests that 1-2 hrs. is required to optimize the proportion of MS that take up protocells for all three protocell formulations (Tables 1-3 in appendix). Viability remains relatively high at 1 hour incubation for all three formulations using a protocell concentration of 125 ug/mL. Although uptake significantly increases with increasing concentration for DOPC-PEG protocells, the viability dramatically drops for concentrations over 250 ug/mL (Figure 16A). The maximum percentage of MS taking up DOPC-DOTAP particles at 1000 ug/mL was significantly higher than for DOPC-PEG particles, but with a more substantial decrease in viability (Figure 16B). DOPC-DOPS particles had the best overall performance with respect to uptake by MS, combining high uptake (80%) with viability superior to that observed in DOPC-DOTAP for the same incubation conditions (85% vs. 50%) (Figure 16C).

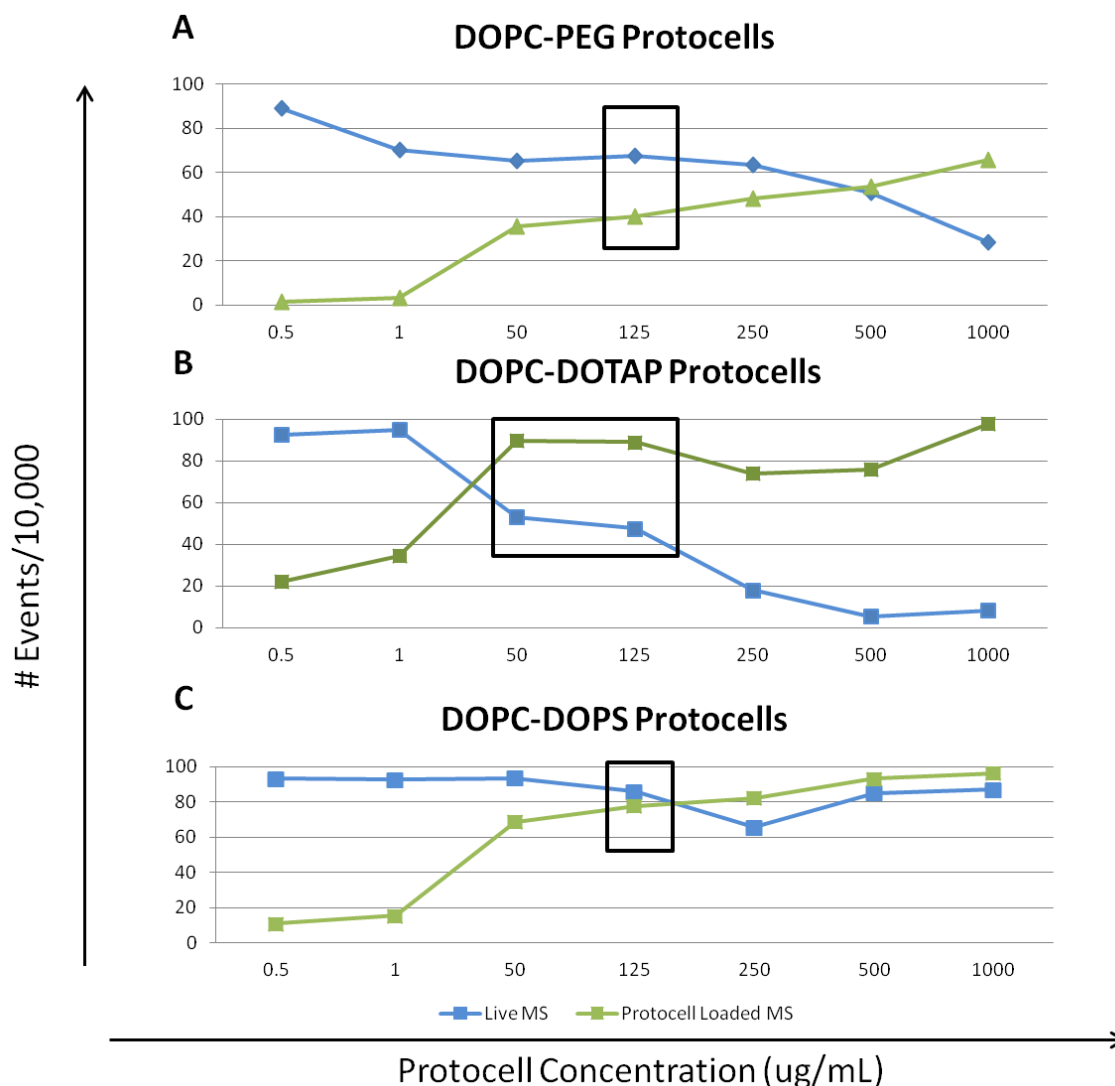


Figure 16: Fraction and Viability of MS Loaded with Protocells. Flow cytometric analysis of cell viability (detected by Live/Dead violet staining) and proportion of MS with protocells after 1 hr incubation at 37°C under 5% CO₂. Viability and protocell labeling are optimized at 125 ug/mL in all three protocell formulations. DOPC-PEG protocells were somewhat cytotoxic (~60% viability at low concentrations) and less effectively taken up by MS compared to other protocell formulations (A). Uptake efficiency in DOPC-DOTAP particles was optimal, though these particles are significantly cytotoxic (B). DOPC-DOPS protocells are the most compatible with MS without compromising cell uptake efficiency (C).

5.3.2 Biodistribution of Different Protocell Formulations after Direct Injection versus MS Adoptive Transfer

The biodistributions of the DOPC-DOPS, DOPC-DOTAP, and DOPC-PEG protocells, loaded into MS, were compared *in vivo* in order to investigate whether the protocell formulation influences MS migration post adoptive transfer. Flow cytometric analysis of the digested organs suggests that there is a difference in biodistribution of MS that is dependent on the formulation of protocell ingested. The tumor-to-organ ratio of protocell-positive cells in tumors relative to liver, kidney or spleen are plotted in Figure 17. MS did not significantly improve DOPC-PEG tumor delivery (Figure 17A). However, tumor-to-liver and tumor-to-spleen ratios of DOPC-DOPS protocells were enhanced by MS-mediated delivery relative to direct injection (Figure 17B). MS-mediated delivery also appears to improve DOPC-DOTAP protocell delivery to the tumors, relative to direct injection (Figure 17C). These data were helpful in designing the final SPECT imaging experiment, but the group size was too small (N=2 for PyMT and N=1 for FVB) for statistical significance to be evaluated. Cryosections of the second half of the tumors confirm an association of both MS-mediated and directly injected protocells (Figure 18). As in the MS-mediated delivery of PKH26 (discussed in section 4.3.4), the protocells appear to accumulate in branched regions of the tissue with low nuclear staining (Figure 18). The DOPC-DOPS protocells have some association with DAPI staining in these low DAPI branched regions (Figure 18 B&H) to a greater extent than was seen with DOPC-DOTAP

(Figure 18 C&I) or DOPC-PEG (Figure 18 A&G). The low nuclear staining branched regions were confirmed by H&E staining (Figure 18 D-F and J-L).

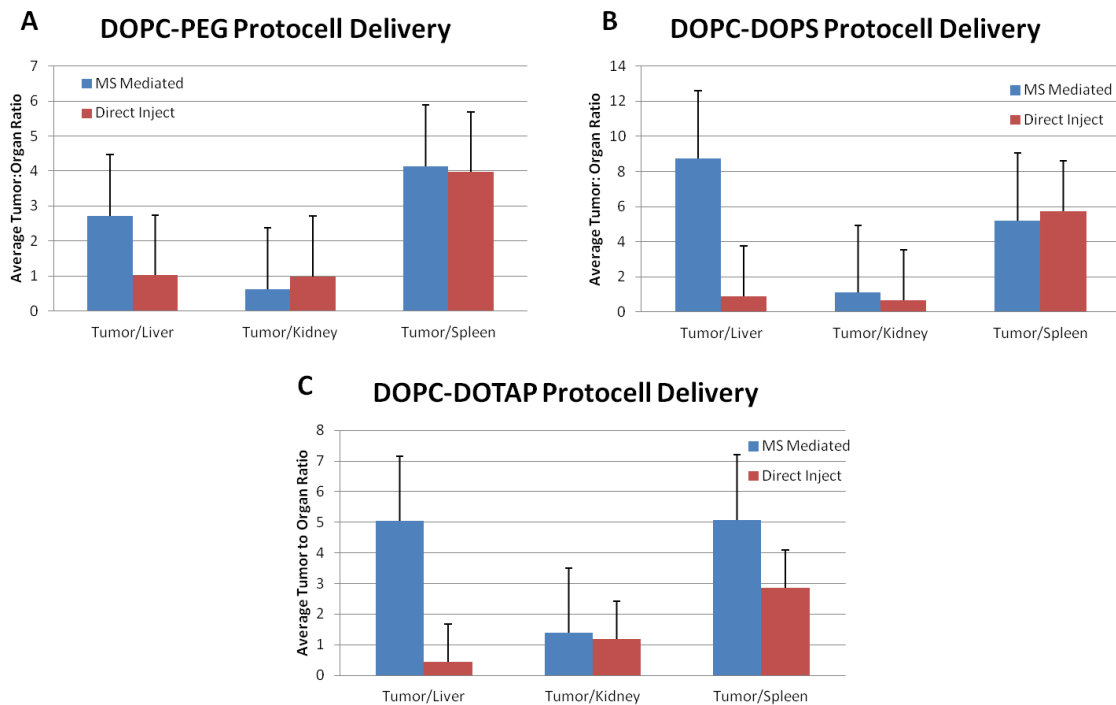


Figure 17: Biodistribution of Protocell Loaded MS. MS were loaded with different formulations of protocells (DOPC-PEG, DOPC-DOTAP and DOPC-DOPS) and adoptively transferred into PyMT mice. The MS were circulated in vivo for 24 hrs. prior to digestion of the organs, followed by flow cytometric analysis of the proportion of DyLight 650 labeled protocells in the tumors, liver, kidneys and spleen. The ratio of signal in tumors relative to liver, kidney and spleen are shown. MS did not significantly improve DOPC-PEG tumor delivery (A). Tumor association of DOPC-DOPS protocells was enhanced compared to liver and spleen by MS-mediated delivery (B). MS also improved DOPC-DOTAP particle delivery to the tumors (C).

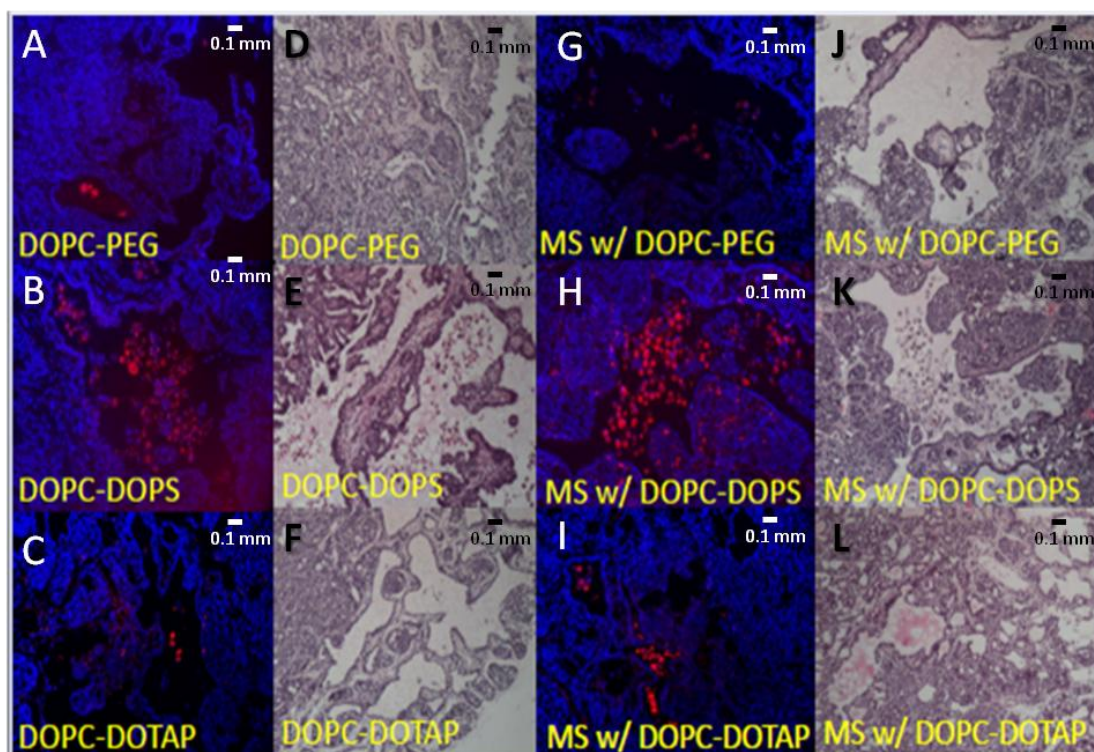


Figure 18: Visual Confirmation of Protocell Delivery to tumors. Five micron cryosections from the second and third right mammary tumors after IV injection of either MS loaded or directly injected DOPC-DOPS protocells. The cryosections were prepared from the same tumors analyzed in Figure 17 after 24 hrs. circulation *in vivo*. The protocells were imaged in the Rhodamine channel at 20X (red) and the tissue was stained with DAPI to illuminate the nuclei (blue) (A-C and G-H). The corresponding sections were stained with H&E and confirm low nuclear staining of the protocell associated branched regions of tissue (D-F and J-L). Protocell delivery 500 μ m into the tumors is visually confirmed (A-C and G-I) and mimics the MS-mediated biodistribution of PKH26 shown in Figure 14. All scale bars measure 0.1 mm.

5.3.3 SPECT/CT Imaging of DOPC-DOPS Protocell Biodistribution after

Direct Injection, MS Adoptive Transfer, and BMDM Adoptive Transfer

To more thoroughly test the efficiency of immune cell mediated drug delivery to mammary epithelial tumors, the biodistribution of radiolabeled protocells was imaged *in vivo* by SPECT/CT imaging. Specifically, the biodistribution of protocells delivered by direct IV injection was compared to delivery by MS adoptive transfer, in tumor (PyMT) and non-tumor (FVB) mice. Additionally,

protocell delivery by BMDM adoptive transfer was imaged in non-tumor bearing (FVB) mice.

SPECT/CT images demonstrate that MS-mediated DOPC-DOPS protocell distribution is primarily localized to the liver, kidneys and spleen of both PyMT and FVB mice (Figure 19). The average uptake of protocells by the normal mammary tissue of FVB mice (1 %ID/g) is significantly lower ($p < 0.001$) than the average protocell uptake observed in the mammary tumors of PyMT mice (2 %ID/g) after 24 hrs. circulation (Figure 23). One PyMT mouse was not properly injected and most of the sample was administered into the tail tissue, which perhaps fortuitously resulted in a more specific association with tumors (Figure 20).

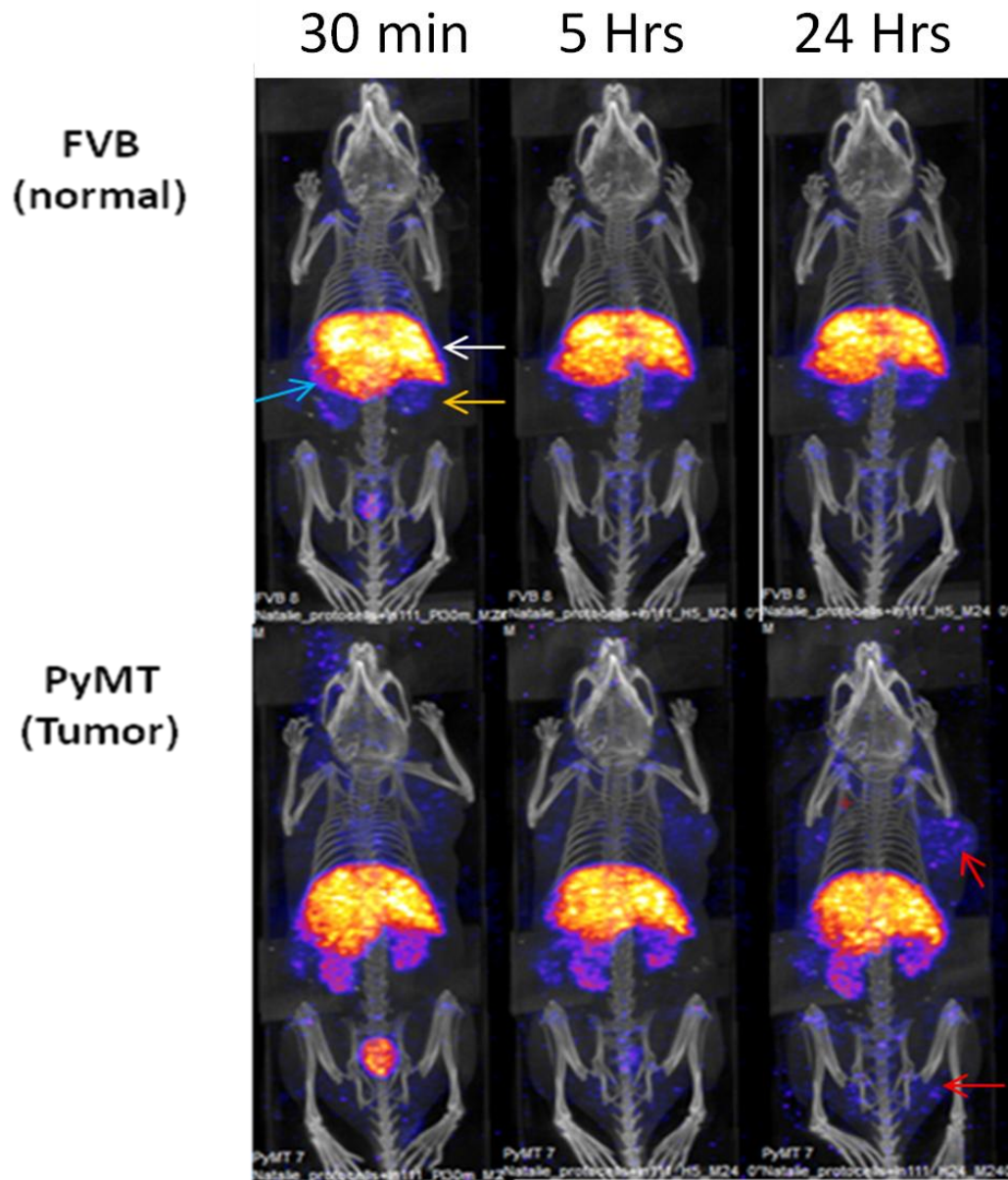


Figure 19: Biodistribution of MS Loaded with DOPC-DOPS Protocells. MS were co-incubated with DOPC-DOPS protocells labeled with Indium-111 and DyLight 650 and adoptively transferred into PyMT and FVB mice. SPECT/CT images suggest that protocell distribution is localized to the liver (white arrow), kidneys (yellow arrow) and spleen (blue arrow) of both PyMT and FVB mice. The protocells do not visibly accumulate in the normal mammary tissue of FVB mice (top), but do accumulate in the tumors of PyMT mice (red arrows) over 24 hrs. circulation.

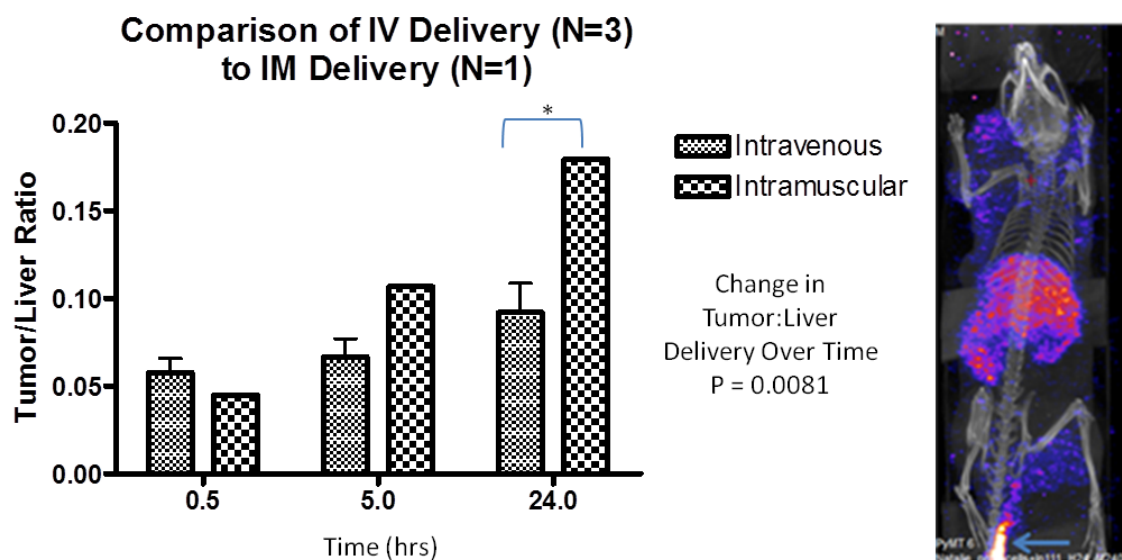


Figure 20: Quantitative Confirmation of MS-mediated DOPC-DOPS Protocell Biodistribution. Post SPECT/CT quantitative analysis of MS-mediated protocell distribution was assessed by quantifying the injected dose of DOPC-DOPS protocells in mammary/tumors, liver, kidneys and spleen using a gamma counter. The average injected dose was normalized to muscle. One PyMT mouse was not injected properly (image shown on right, blue arrow), but resulted in a more specific association with tumors (left).

Qualitatively, directly injected DOPC-DOPS protocells mimic the biodistribution of MS-mediated protocell distribution, in that protocell distribution is again primarily localized to the liver, kidneys and spleen within 30 min. and remains in these organs over 24 hrs (Figure 21). As observed in the case of MS adoptive transfer, the uptake of directly-injected protocells by normal mammary tissue of FVB mice (1 %ID/g average) is significantly lower ($p < 0.0056$) than the uptake by mammary tumors in PyMT mice (2-2.5 %ID/g average) over 5 and 24 hrs. circulation (Figure 23).

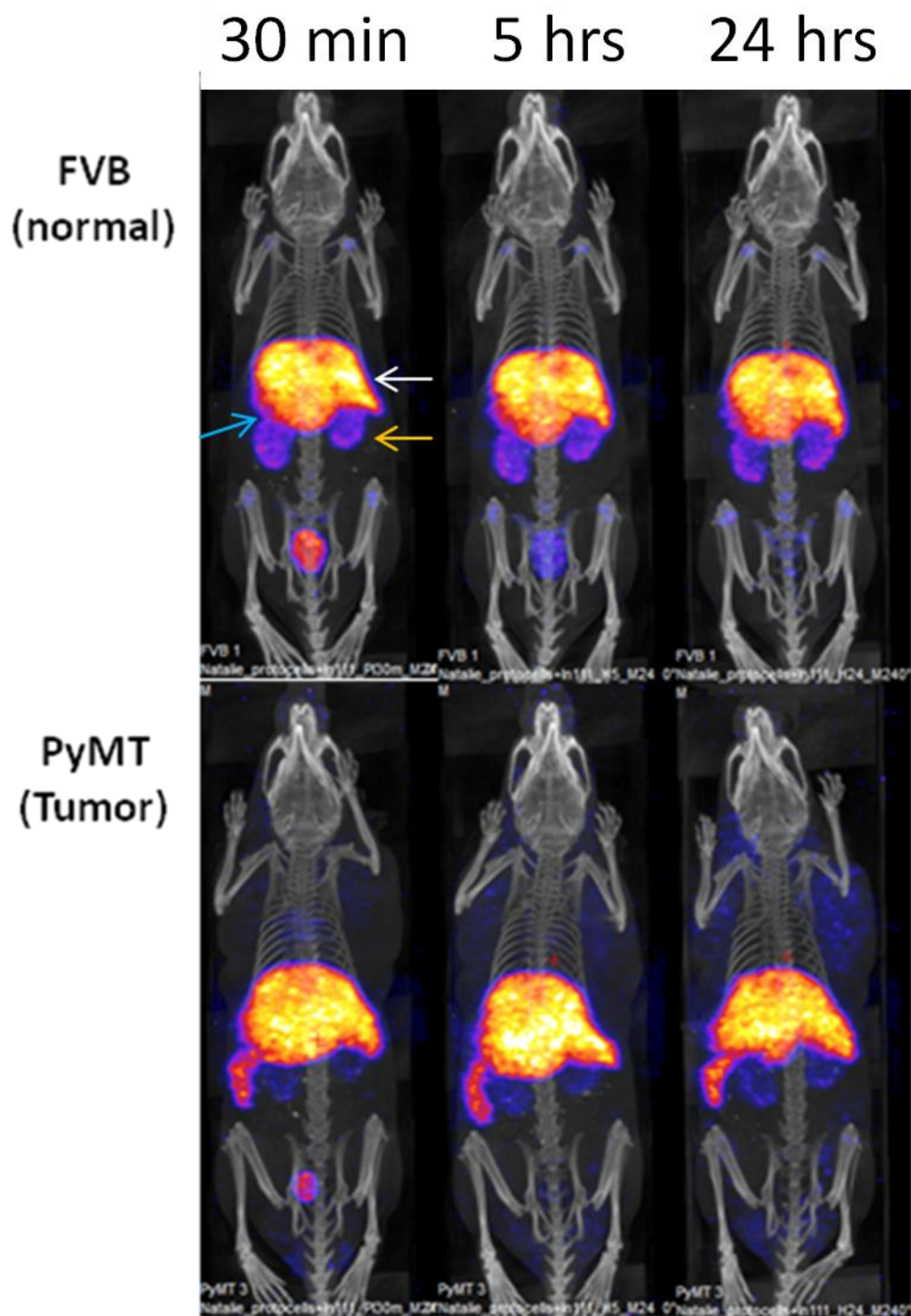


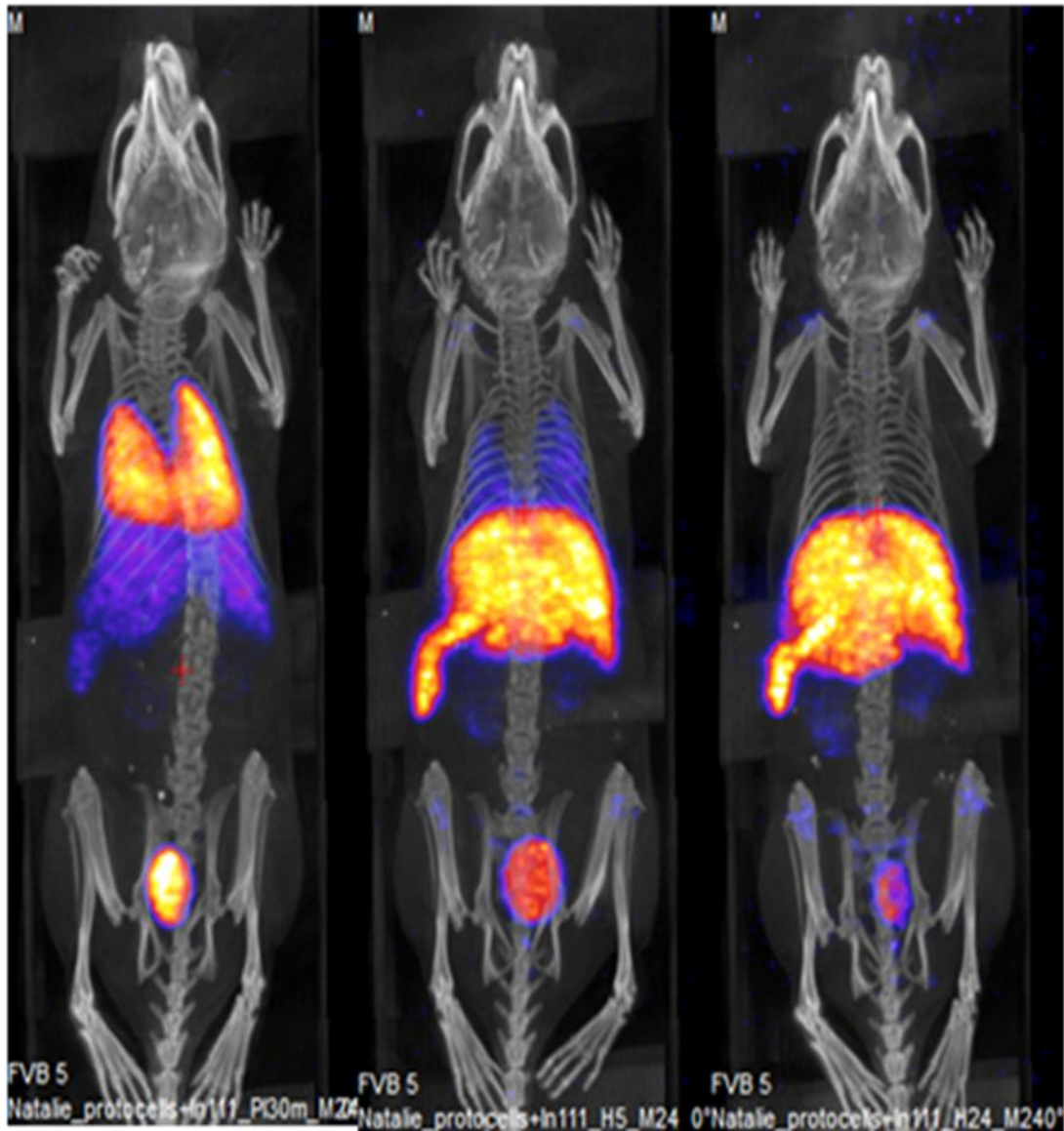
Figure 21: Biodistribution of Directly Injected DOPC-DOPS Protocells. DOPC-DOPS protocells labeled with Indium-111 and Dylight 650 were injected into PyMT and FVB mice. SPECT/CT images suggest that protocell distribution is localized to the liver (white arrow), kidneys (yellow arrow) and spleen (blue arrow) within 30 min. and remains in these organs over 24 hrs. The protocells do not accumulate in the normal mammary tissue of FVB mice, but do accumulate in PyMT tumors after 24 hrs. (red arrows).

BMDM mediated protocell biodistribution is significantly different from that observed after MS adoptive transfer. SPECT/CT images show that protocell-loaded BMDMs rapidly localize to the lungs, within 30 min. of injection (Figure 22). Protocell-loaded BMDMs then migrate to the liver, kidneys, and spleen over 24 hrs. The circulation time-dependence of the biodistribution of BMDM was significant for all cohorts ($p < 0.0001$). In FVB mice (normal mammary tissue), the uptake of protocell loaded BMDMs by mammary tissue is significantly lower compared to the uptake of protocells delivered by direct injection or MS adoptive transfer with $p < 0.01$ at 30 min. and 5 hrs. and $p < 0.05$ at 24 hrs., and MS uptake was significantly lower with $p < 0.05$ (Figure 23).

30 min

5 hrs

24 hrs



FVB (normal)

Figure 22 Biodistribution of BMDM Loaded with DOPC-DOPS Protocells. BMDM were co-incubated with DOPC-DOPS protocells labeled with Indium-111 and Dylight 650 and adoptively transferred into FVB mice. SPECT/CT images suggest that protocell distribution is localized to the lungs within 30 min. of injection. The sample migrates to the liver, kidneys and spleen over 24 hrs. The protocells loaded BMDMs do not accumulate in the normal mammary tissue of FVB mice.

The quantified mammary ROI uptake suggests a marked increase in tumor uptake after 24 hrs. in both MS-mediated and directly injected DOPC-DOPS protocells (Figure 23C). In all cases, the majority of protocells ended up in the liver and kidneys (Figure 24-26). The quantified mammary ROI signal suggests a significant accumulation in the lungs after 30 min. circulation by BMDM mediated delivery compared to the other cohorts (Figure 27). Protocells accumulated in the bones of FVB mice more significantly than in PyMT mice (Figure 27). All cohorts demonstrated initial uptake by the heart that decreased over time. The BMDM at 30 min. post injection showed the highest heart uptake of all cohorts (Figure 29).

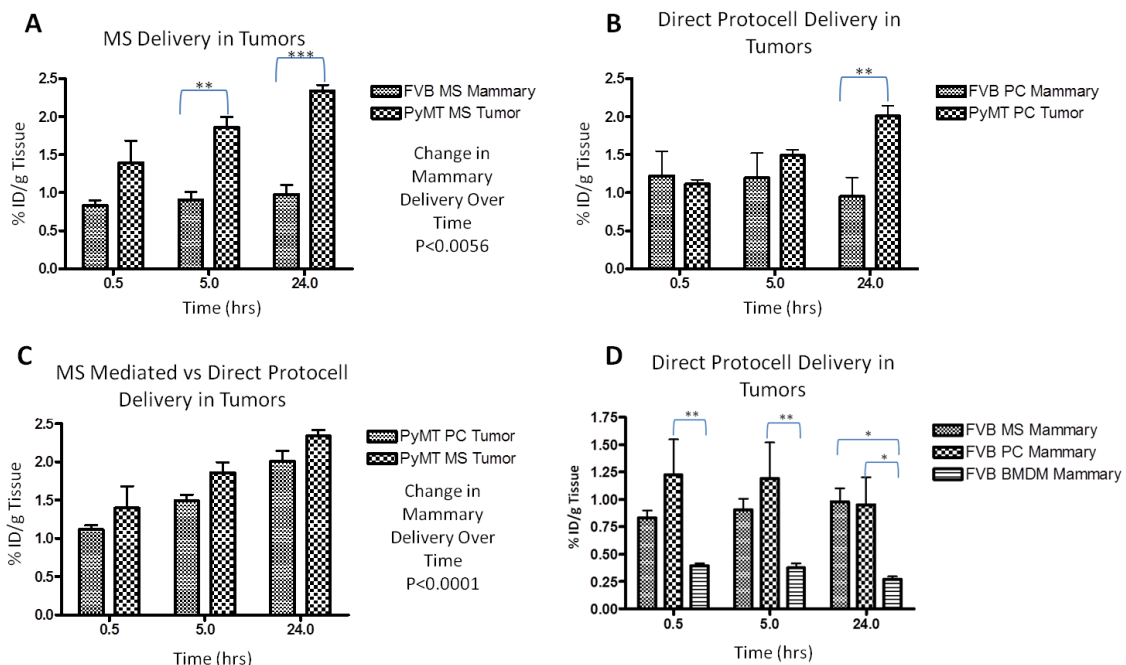


Figure 23: SPECT/CT Analysis of Protocell Delivery to Tumor/Mammary Tissue.

MS loaded or direct DOPC-DOPS protocells labeled with Indium-111 and Dylight 650 were injected into PyMT and FVB mice. The percent injected dose per gram of tissue (%ID/g) was determined from tumor ROIs and two-way analysis of variance (ANOVA) of each group was carried out analyzed by time and injectate. MS-mediated protocell delivery improved significantly over time (A) and showed slightly higher tumor uptake compared to directly injected protocells, but the difference was not significant (C). Both directly injected and MS-mediated protocell delivery is enhanced in tumors compared to normal mammary tissue (A & B). There was significantly less effective protocell delivery to mammary tissue in FVB mice mediated by BMDM compared to MS-mediated or directly injected protocells (D).

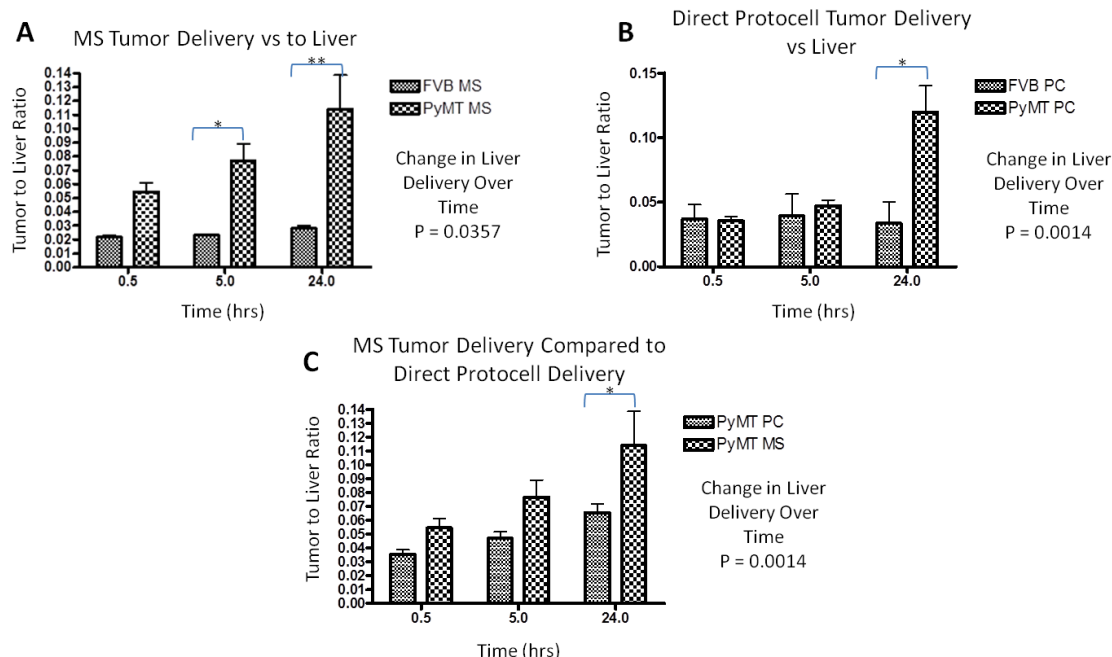


Figure 24: SPECT/CT Analysis of Protocell Delivery: Tumor-to-Liver Ratio. MS loaded or direct DOPC-DOPS protocells labeled with Indium-111 and Dylight 650 were injected into PyMT and FVB mice. The tumor-to-liver ratio was computed, and two-way ANOVAs of each group analyzed by time and tumor to organ ratio per injectate. The tumor-to-liver ratio achieved using MS-mediated protocell delivery to tumor versus liver was higher in PyMT mice compared to FVB at all time points (A). MS delivery resulted in an increasing tumor-to-liver ratio as a function of time in PyMT mice, although the trend was not matched in FVB mice (B). Direct injection of protocells resulted in similar tumor-to-liver ratios at 30 min. and 5 hrs. when comparing PyMT and FVB mice. However, at 24 hrs. the tumor-to-liver ratio was significantly higher in PyMT mice (B). MS-mediated delivery was significantly higher than direct injection at 24 hrs (C).

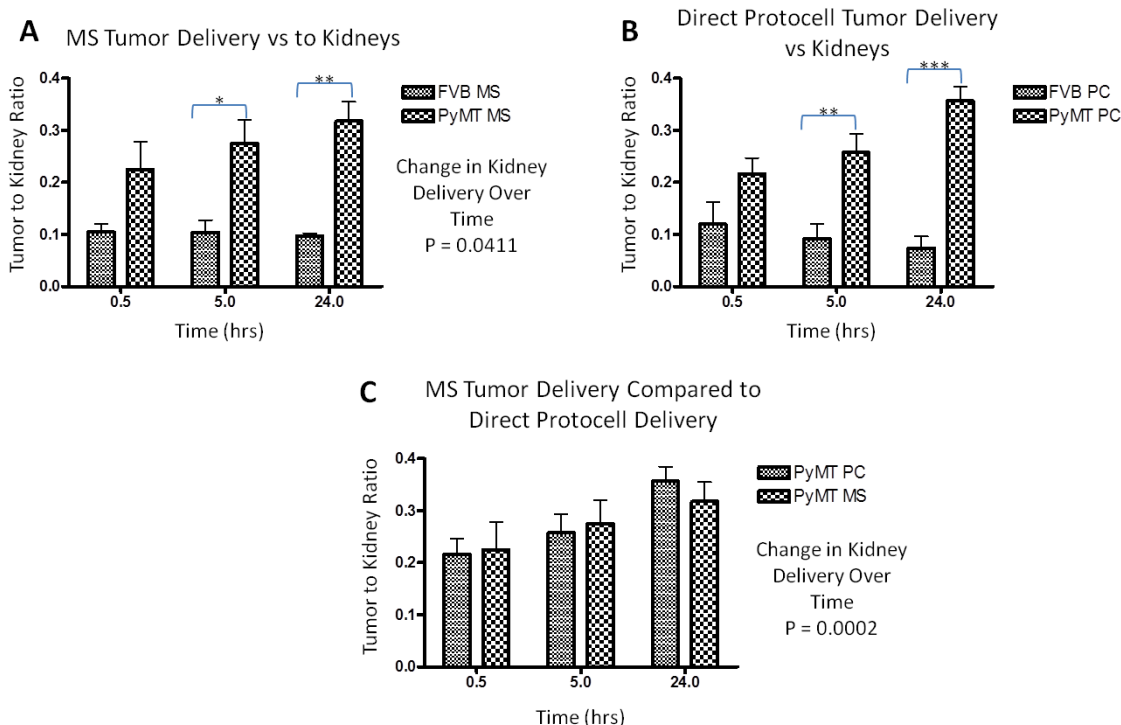


Figure 25: SPECT/CT Analysis of Protocell Delivery: Tumor-to-Kidney Ratios.

DOPC-DOPS protocells labeled with Indium-111 and Dylight 650 were loaded into MS for adoptive transfer or directly injected into PyMT and FVB mice. The tumor-to-kidney ratio was computed and we performed two-way ANOVAs of each group analyzed by time and tumor to organ ratios per injectate. The tumor-to-kidney ratio obtained after MS-mediated tumor delivery was higher in PyMT mice compared to FVB with statistical significance achieved at 5 hrs circulation (A). Directly injected protocells also resulted in a higher tumor-to-kidney ratio in PyMT mice (for both MS-mediated delivery and direct injection), but this trend was not observed in FVB mice (B). MS-mediated protocell delivery did not result in a statistically significant difference in the tumor-to-kidney ratio when compared to direct injection (C).

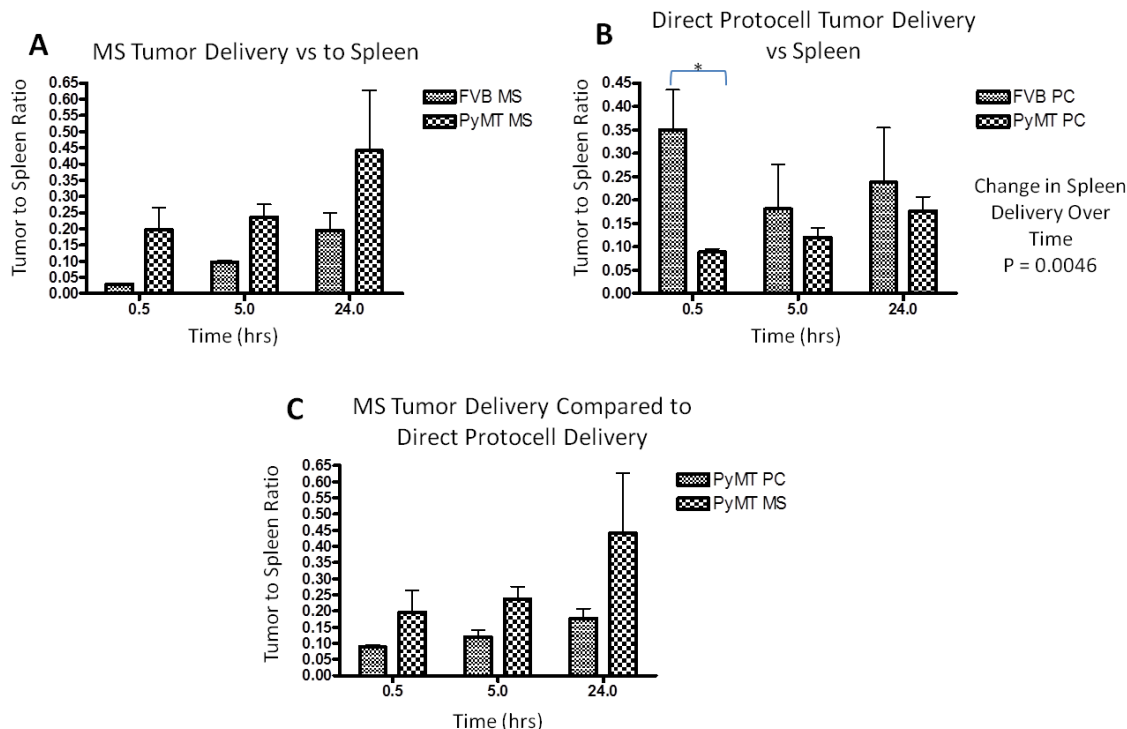


Figure 26: SPECT/CT Analysis of Protocell Delivery to Spleen. Indium-111 and Dylight 650 labeled DOPC-DOPS protocells were loaded into MS for adoptive transfer or direct injection into PyMT and FVB mice. The tumor-to-spleen ratio was determined at each time point and two-way ANOVAs of each group were performed by time and injectate. With respect to the tumor-to-spleen ratio, MS-mediated tumor delivery was slightly better in PyMT mice compared to FVB (A), but the difference was not significant. Directly injected protocells resulted in a higher mammary-to-spleen ratio in FVB mice relative to PyMT mice after 30 min. circulation (B). The tumor-to-spleen ratios achieved by MS-mediated protocell delivery are generally superior to direct injection, but the difference is not statistically significant (C).

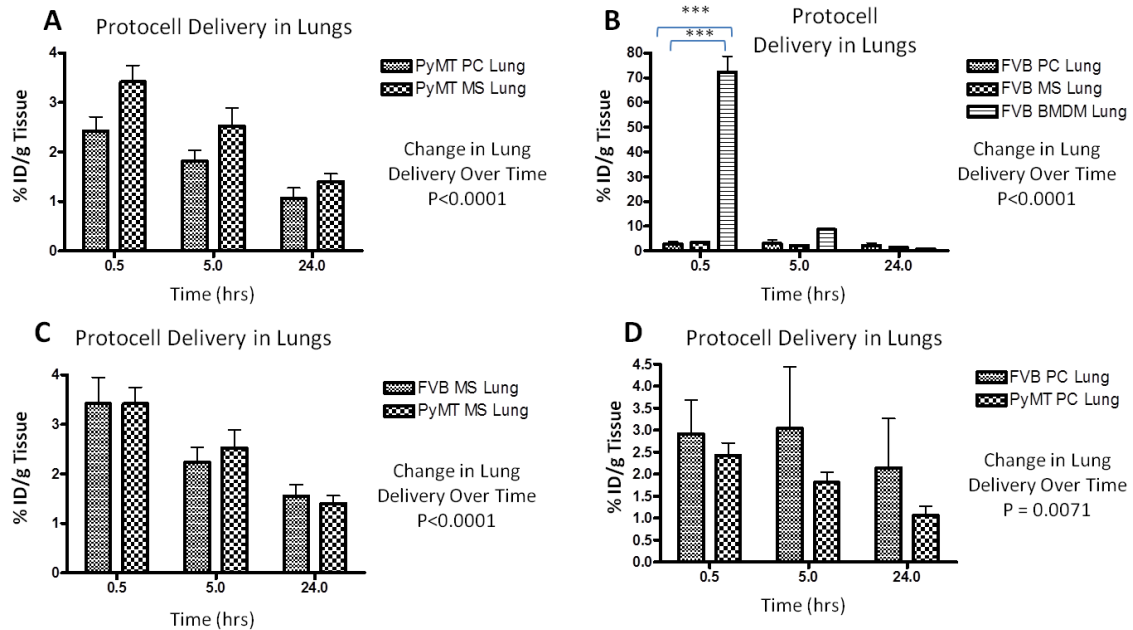


Figure 27: SPECT/CT Analysis of Protocell Delivery to Lungs. DOPC-DOPS protocell labeled with Indium-111 and Dylight 650 were loaded into MS for adoptive transfer or direct injection into PyMT and FVB mice. ROIs of the lung were analyzed and two-way ANOVAs of each group analyzed by time and injectate. MS-mediated protocell delivery to the lungs is not significantly different from directly injected protocells (A). However, BMDM delivered protocells accumulated more significantly in the lungs of FVB mice after 30 min. circulation in comparison to both MS-mediated delivery and direct injection of protocells.(B). Both MS-mediated delivery and direct injection of protocells resulted in delivery to lung that was not significantly different in PyMT mice compared to FVB (C & D). Both MS-mediated and direct protocell delivery to the lungs are not significantly different between genotypes (C&D).

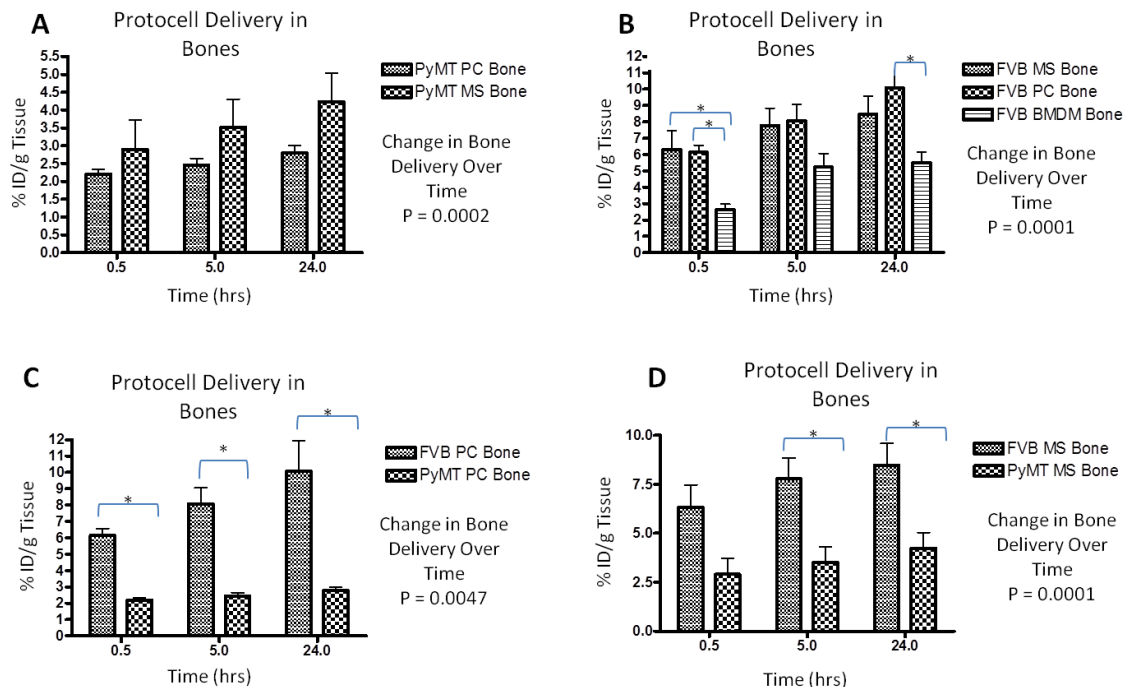


Figure 28: SPECT/CT Analysis of Protocell Delivery to Bones. DOPC-DOPS protocell labeled with Indium-111 and Dylight 650 were loaded into MS for adoptive transfer or direct injection into PyMT and FVB mice. ROIs of the lung were analyzed and two-way ANOVAs of each group analyzed by time and injectate. MS-mediated protocell delivery resulted in higher bone uptake relative to direct injection in PyMT mice, but the difference was not significant (A). Both MS-mediated and directly injected protocells accumulated more significantly in the bones of FVB mice compared to BMDM delivery at 30 min (B). Both MS-mediated and direct protocell delivery to the bones is significantly different between genotypes with FVB mice showing significantly higher bone uptake (C & D).

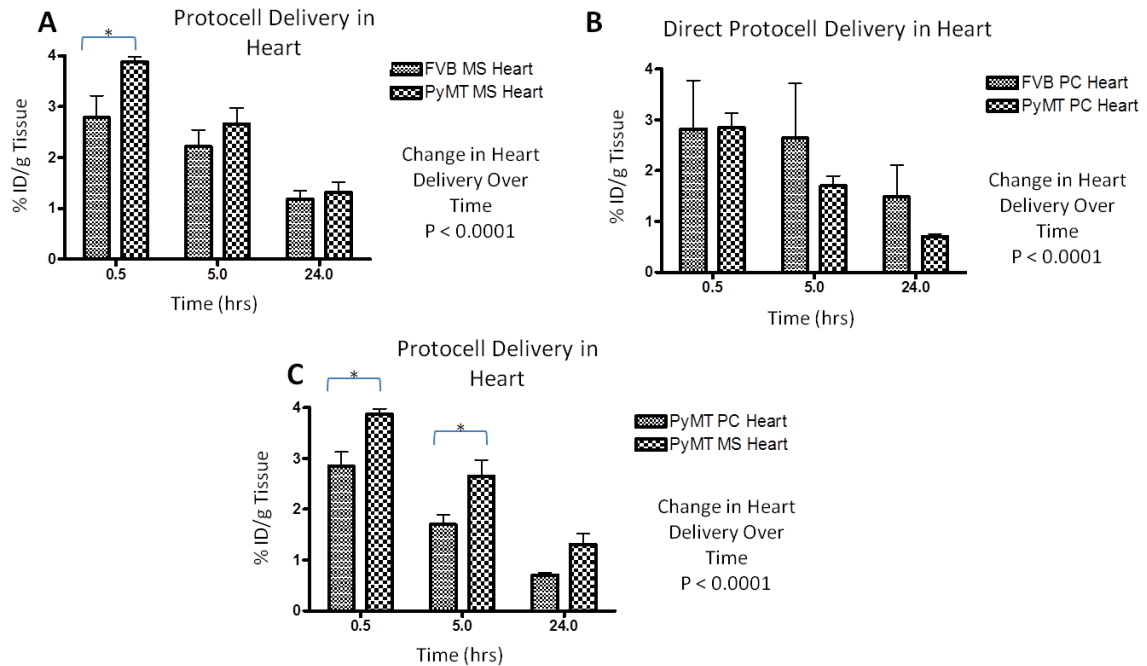


Figure 29: SPECT/CT Analysis of Protocell Delivery to Heart. DOPC-DOPS protocell labeled with Indium-111 and Dylight 650 were loaded into MS for adoptive transfer or direct injection into PyMT and FVB mice. ROIs of the lung were analyzed and two-way ANOVAs of each group analyzed by time and injectate. MS-mediated protocell delivery was significantly higher in PyMT mice compared to FVB after 30 min. circulation (A) and the signal declined over 24 hrs. Direct protocell delivery to the heart is not significantly different between genotypes and the signal declines over 24 hrs (B). MS-mediated protocell delivery to the heart was significantly higher than direct protocell delivery at 30 min. and 5 hrs. circulation (C).

Chapter 6

Discussion

6.1 INTRODUCTION

Nanotherapeutics are substantially contributing to cancer therapies and emerging as powerful treatment modalities for breast cancer. Some of the common issues concerning conventional chemotherapeutics, such as limitations in achievable doses within the tumor and cancer cell resistance to molecularly targeted chemotherapeutics, are mitigated by nanomaterials. Targeted nanoparticles, for example, enter cancer cells by receptor mediated endocytosis rather than passive diffusion through the cell membrane, thus avoiding P-glycoprotein recognition and subsequent efflux back out of the cell (Larsen 2000). The versatility and biocompatible properties of nanotechnology combined with advancements in our understanding of tumor growth and invasion has allowed for a rapid expansion of the field of nanomedicine with copious developments of new nanoparticles for the diagnosis and treatment of cancer. Polymeric micelles, for example, resolve the issue of solubilizing typically hydrophobic chemotherapeutics in biocompatible aqueous media. These water soluble amphiphilic block copolymers assemble into nanoshells with a hydrophobic core region which stabilizes the hydrophobic drug, rendering the drug water-soluble and allowing for IV administration (Adams 2003). A polymeric micelle formulation of Paclitaxel demonstrates current clinical application of this technology, as it is commonly used to treat patients with advanced refractory malignancies (Kim 2004).

Investigations into chemotherapeutic transport phenomena are inspiring researchers to reassess nanoscale drug carrier designs to overcome biological barriers while enhancing drug accumulation within tumors and incorporating controlled release mechanisms for depositing drug payloads. Liposomes are a popular design effort to meet the goals of drug encapsulation, targeting, and release. Liposomes are self-assembling colloidal structures of lipid bilayers that can be modified with targeting ligands and different lipid compositions to improve targeting while protecting the drug en route. This technology is successfully used in cancer therapy with Doxorubicin and Anthracyclines, which are commonly used for treating metastatic breast cancer (Rivera 2003; Markman 2006).

Protocells are another class of nanocarrier that modifies liposome technology with mesoporous silica particles to provide a versatile platform for addressing the multiple challenges of targeted delivery. The mesoporous silica core provides a high surface area that enables a higher drug loading capacity than is afforded in traditional liposomes of similar size. Doxorubicin loading of protocells showed a 1,000-fold increase in loading capacity compared to similarly sized liposomes (Ashley 2011). The charged silica core stabilizes the phospholipid bilayer resulting in greater stability and increased bilayer fluidity, which improves the efficiency and targeting specificity of targeting ligands at a minimal ligand concentration (Ashley 2011). Protocells also incorporate a pH dependent release mechanism whereby low pH destabilizes the phospholipid bilayer, allowing the encapsulated drug to be released.

Combining multimodal delivery platforms with a means of active delivery will significantly enhance the performance of drug carriers in cancer therapeutics. Advancements in immunotherapy and tumor immunology have elucidated a heterogeneous population of circulating mononuclear cells that play a significant role in tumor inflammation and infection (Wynn 2013). Mononuclear phagocytes in particular are extensively recruited during inflammation and are known to accumulate in hypoxic regions of tumors, including breast carcinomas, due to the cytokines released by tumor cells in response to hypoxia (Leek 1996). This is an advantage for using mononuclear phagocytes to distribute cancer therapeutics throughout the interior of the tumor because hypoxia is typically widespread in malignant tumors due to the disorganized vascular architecture and poor lymphatic drainage (Batrakova 2011; Kobayashi 2014). Therefore, we hypothesized that circulating mononuclear cells are effective biologically active carriers of cancer nanotherapeutics and investigated merging immunotherapy with targeted drug delivery of protocell multimodal nanotherapeutic platforms.

6.2 DISCUSSION OF RESULTS AND CONCLUSIONS

Mononuclear cells were isolated from the spleen, a known reservoir of mononuclear cell that expands in cancer (Cortez-Retamozoa 2012). Our results demonstrate isolation of viable MS (Figure 1) that do not have uniform nuclear morphology, a morphological feature of mature macrophages, and the nucleus to cytoplasm ratio is much larger than is typically seen in mature macrophages (Figures 1 and 2). A significant proportion of MS express Ly6C/G (Gr1) (Figure

3), which is indicative of inflammatory monocytes, a heterogeneous population that lacks classic features of mature macrophages and dendritic cells and is known to expand in during cancer inflammation and infection (Wynn 2013). TAMs are also prominently featured in many inflammatory responses to tumors and commonly express F4/80 and CD11b, so we investigated the efficacy of MS-mediated drug delivery in comparison with BMDM (Balkwilla 2012). BMDM were shown to be strongly F4/80 and CD11b positive, as shown in Figure 3, suggesting a mature macrophage phenotype (Hume 2002). Both MS and BMDM are phagocytic (Figures 4 and 5), demonstrating the capacity to take up particulates on order of the typical size of nanotherapeutics (Cheng 2012). MS and BMDM tumor targeting *in vivo* was assessed by adoptive transfer into tumor bearing PyMT mice and compared against FVB mice with normal mammary tissue. SPECT/CT analysis of IV injected MS suggests about a three-fold larger proportion of MS migrate to tumor tissue versus normal mammary tissue (Figure 6-8), which is suggestive of a prevalent inflammatory responsive subset of the MS population. Alternatively, BMDM directly migrate to the lungs initially, followed by a gradual migration into common filtering organs, such as the liver, kidneys, and spleen (Figure 10). There was no detectable signal of adoptively transferred MS in the lungs, which is suggestive of a primarily immature mononuclear population of monocytes rather than differentiated macrophages (Figure 6-8). Further characterization of BMDM is required to elucidate why there is such a specific migration to the lungs and not an affinity for the tumors. Typically circulating macrophages are thought to migrate to tumors (Movahedi

2010), so further immunological staining for other cell surface markers, such as MHC classes 1 and 2 receptors, might indicate why BMDM do not migrate to tumors.

A more intriguing aspect of MS biodistribution observed *in vivo* is that MS infiltration into tumor tissue is impacted by the duration of incubation at 37°C prior to adoptive transfer. Tumor targeting appeared to be enhanced the longer the injectate incubated at 37°C, however cytokine array analysis revealed no detectable activation state of the injectate population prior to adoptive transfer (Figure 11). There appeared to be no significant change in cell surface expression markers, but there was a slight increase in phagocytic behavior, as observed through flow cytometric quantification of PKH26 micelle uptake (Figure 12). Several subtle differences in MS population dynamics were observed in the size and granularity of cells, as seen by flow cytometry. The lymphocyte and monocyte populations diverged into two subsets. The lymphocytes were smaller in size and the monocytes were less granular (Figure 13). A third population of small size and high granularity appears after four hours incubation at 37°C, which suggests a possible differentiation of myeloid cells into tumor suppressor cells that are highly granular. These are perhaps polymorphonuclear myeloid derived suppressor cells, which are consistently the dominant population of expanding mononuclear cells in tumor-bearing hosts (Wynn 2013). Further characterization of the cell population as a function of time incubated at 37°C is required to elucidate the link between sample preparation and *in vivo* biodistribution.

In order to determine whether MDSC were the subset of the MS population that targeted the tumors, we attempted to purify Ly6C (Gr1)/CD11b positive cells using mouse monocyte enrichment kits (StemCell). We demonstrate enrichment of CD11b⁺ MS by negative selection and further enrichment of Ly6C (Gr1) positive cells through a positive selection kit, however the yield decreased by an order of magnitude, which proved this method impractical for MDSC isolation from the spleen (Figure 15). Therefore, we investigated the tumor affinity of the phagocytic subset of MS as possible nanotherapeutic carriers. MS were labeled with PKH26 fluorescent micelles and tracked *in vivo* post adoptive transfer into PyMT mice. The majority of the MS population took up PKH26 micelles, the bulk of which were phagocytosed by cells exhibiting macrophage forward and side scatter characteristics (Figure 4). This large percentage of phagocytic MS reflects previous studies estimating up to 8% of the mononuclear fraction of blood obtained from patients with lymphocytic leukemia to be phagocytic (Zucker-Franklin 1974).

To confirm that MS can carry cargo to tumors *in vivo*, we adoptively transferred PKH26 loaded MS into PyMT mice. Upon cryosectioning the tumors, we observed delivery of PKH26 loaded MS to tumors (Figure 14). There appears to be an association with pockets of little to no DAPI nuclear staining and very highly disorganized WGA. WGA is an agglutinin protein, or lectin, that binds to N-acetyl-D-glucosamine and Sialic acid. Metastatic cancer cells are known to express a high density of sialic acid-rich glycoproteins (Narayanan 1994). Also, WGA has been shown to recognize lectin groups significantly more

prevalently in hypoxic lesions found in DCIS than in non-hypoxic regions and the staining is primarily cytoplasmic (Barreto de Melo Rêgo 2013). MS are known to have an affinity for hypoxic regions of tumors, so it is possible that MS target hypoxic lesions of the tumor (Movahedi 2010). However, further investigation is required in order to make any strong conclusions regarding this phenomenon. For example, histological staining of sialic acid and glycoproteins would confirm whether the low DAPI regions observed are associated with an increase in sialic acid and glycoprotein secretion or cell surface expression compared to normal mammary tissue. The lack of DAPI stained nuclei observed in these high WGA stained regions combined with the aggregated morphology of WGA staining possibly suggests WGA staining mucin glycoprotein, which are heavily secreted in metastatic tumors and are often localized to luminal regions that have low cell density. High mucin secretion is thought to provoke immune responses in patients with carcinomas, which might MS association with these regions of the tumor (Varki 2009).

Having established MS tumor targeting *in vivo* post adoptive transfer, we next investigated the capacity of MS to transport cargo to tumors *in vivo*. We chose to incorporate protocells as a mock cargo because they are actively being pursued as a multicomponent targeted nanotherapeutic (Ashley 2011). We demonstrate the capacity of MS to uptake protocells of different lipid compositions (Figure 16, Tables 1-3 in appendix). Lipid formulation directly impacted MS viability and protocell uptake. Charged nanoparticles, for example, are known to rapidly be taken up by mononuclear phagocytes more readily

compared to neutral particles (Juliano 1975; Lee 1992). Positively charged particles are phagocytosed by mononuclear phagocytes to a greater extent than negatively charged particles, as was seen in retroviral uptake studies comparing mononuclear phagocyte uptake of positively versus negatively charged nanoparticles that were homogenized with antiretroviral drugs. Mononuclear cell uptake of positively charged nanoparticles was two-fold higher than with negatively charged particles (Nowacek 2009). Therefore, positively charged DOPC-DOPS protocells were compared against negatively charged DOPC-DOTAP protocells. DOPC-DOPS protocells were readily taken up by MS and did not significantly impact cell viability at low concentrations, on the order of 125 ug/mL (Figure 16). DOPC-DOTAP, negatively charged, particles were cytotoxic at high concentrations, though particle uptake was enhanced (Figure 16). These results demonstrate that MS can be loaded with a variety of particle formulations, but are most compatible with DOPC-DOPS protocells after incubation for 1 hr at 37°C.

PEG coated nanocarriers are one of the most common particles used for injectable nanotherapeutics because PEG is electrostatically neutral and hydrophilic, which protects the nanocarrier from immune recognition (Katrin Knop 2010). Several PEG carriers have been approved for clinical treatment of metastatic breast cancer (Papaldo 2006). However, PEG particles are likely not compatible with cell mediated therapeutics, as PEG tends to limit cellular uptake (Gbadamosi 2002). Therefore, PEG coated DOPS protocells were compared with DOPC-DOPS and DOPC-DOTAP protocells to assess the efficacy of

evading the immune response extracellularly by PEG or intracellularly by immune cell drug delivery. PEG coated particles did not severely impact cell viability, but particle uptake was less efficient compared to other formulations (Figure 16). These findings support other studies that suggest nanoparticles with PEG coronas are stable and have limited cytotoxicity, but are less readily taken up by mononuclear phagocytes compared to particles without a PEG corona (Batrakova 2011).

The efficacy of MS or BMDM transport of protocells compared to direct injection was assessed *in vivo* by SPECT/CT. The quantified mammary ROIs of the brain, liver, kidneys, bone, heart, spleen, and tumors/mammary glands demonstrate comparable tumor delivery of protocells with MS, compared to directly injected protocells, and not in BMDM (Figure 24), suggesting an immature immune cell phenotype is more desirable for drug transport. The similar performance between direct IV delivery of protocells versus MS-mediated delivery suggest the diffusion properties of charged protocells is on the order of MS recruitment to tumors. However the similar aggregation patterns of both direct and MS-mediated protocells observed in the tumor sections are suggest the protocells are being readily taken up by circulating and/or tissue resident phagocytic cells (Figures 18 & 24). Also, analysis of the tumor to organ ratios of MS-mediated protocell delivery are generally not significantly higher than directly injected protocells. DOPC-DOPS protocells are positively charged, which stimulates uptake by endogenous phagocytic immune cells and might account for the comparability of directly injected protocells with immune cell mediated

protocell delivery. Further histological staining for possible tissue resident phagocytic cells is required to confirm the association of directly injected protocells with phagocytic cells in the tumors.

BMDM are potentially viable candidates for lung therapeutics, which further validates efforts towards harnessing immune cells for targeted therapies. Both interstitial macrophages and lung associated dendritic cells are F4/80 and CD11b double positive, so perhaps the almost immediate association of BMDM with the lungs post adoptive transfer indicates BMDM are more closely differentiated towards the phagocytic cell types typically associated with the lung.

This study demonstrates a potential for immune cell mediated targeted drug delivery that is applicable to the clinic because cell carriers can be harvested from peripheral blood, loaded with particles and re-injected into the patient. Another advantage to utilizing mononuclear cells is that they may be alternatively harvested from bone marrow, which has the advantage of differentiating particular cell types from hematopoietic stem cells and propagating them in culture to obtain higher concentrations of cells that can be adoptively transferred back into the patient once loaded with drug cargo. The directly injected protocell experiments from this study suggest that a third clinical application is potentially available, where the particles are formulated to be taken up by circulating cell carriers in the patient upon IV injection of the particles. Targeting of circulating cells can be achieved by attaching receptor ligands such as folate, fibronectin, mannose or RGD peptide to the particles, which are recognized by mononuclear phagocytes (Batrakova 2011).

6.3 RECOMMENDATIONS FOR FURTHER RESEARCH

Further investigation into MS-mediated therapeutic delivery is required to fully understand the potential. A more efficient purification method, such as FACS sorting, might improve optimization of biodistribution among MS. The interestingly significant improvement in tumor to organ signal observed in the MS-mediated protocell delivery of the PyMT mouse that was not properly injected suggests that immune cell targeting of the tumor might be improved by alternative injection routes, such as intramuscular, peritoneal, or subcutaneous. Investigation into drug release mechanisms should occur in conjunction with optimizing the immune cell carrier population in order to develop a biologically compatible and controllable multimodal platform for immune based targeted therapies with an ultimate goal of testing the efficacy of cell-mediated delivery of drug-loaded protocells on tumor progression. The dynamic vesicle system of mononuclear phagocytes could be exploited as a potential release mechanism for nanotherapeutics because mononuclear phagocytes are known to both generate and store different compounds in intracellular vesicles that are exocytosed at the site of infection (Batrakova 2011). Another option is to elicit an intracellular timed release of calcium in order to induce the immune cell carrier into apoptosis and ultimate release of the cargo (Söllner 1993). This study supports the concept that success in utilizing innate and adaptive immune mechanisms to assist with drug delivery will change our perspective towards clinical treatment strategies.

Appendix

Time Incubated	[Protocell] (ug/mL)	%Live	% Dead	% DOPC-PEG PC Uptake (live)
20 min	1000	46.1	53.9	65.2
	500	8.39	91.6	70.3
	250	8.45	91.6	61.4
	125	23.6	76.4	69.9
	50	24.9	75.1	65.8
	1	90.4	9.55	15.4
	0.5	80.6	19.4	12.9
1 hr	1000	28.5	71.4	65.5
	500	50.9	49.1	53.8
	250	63.6	36.4	48.4
	125	67.5	32.5	40.3
	50	65.4	34.6	35.8
	1	70.4	29.6	3.22
	0.5	89	11	1.59
2 hrs	1000	50.5	4.68	82.6
	500	52	48	69.2
	250	82.2	17.8	46.8
	125	92	8.05	43.9
	50	98	2.03	34.7
	1	95.3	4.68	4.15
	0.5	96.3	3.68	3.17
Time Incubated	[Protocell] (ug/mL)	%Live	% Dead	% DOPC-DOTAP PC Uptake (live)
20 min	1000	9.68	90.3	70.7
	500	25	75	73.7
	250	35.9	64.1	70.8
	125	55	45	60.5
	50	47.3	52.7	60.5
	1	79.3	20.7	31.3
	0.5	91.5	8.46	7.61
1 hr	1000	8.33	91.7	97.9
	500	5.55	94.4	75.9
	250	18	82	74
	125	47.7	52.3	89.1
	50	53.1	46.9	89.7
	1	95	5.04	34.6
	0.5	92.6	7.42	22.2
2 hrs	1000	3.9	7.58	97.1
	500	4.08	95.9	65.5
	250	15.9	84.1	69.5
	125	46.4	53.6	75.5
	50	49.5	50.5	78.8
	1	92.4	7.58	26.5
	0.5	94	6	16.6
Time Incubated	[Protocell] (ug/mL)	%Live	% Dead	% DOPC-DOPS PC Uptake (live)
20 min	1000	2.23	97.8	97.3
	500	49	51	63.7
	250	49.7	50.3	47.2
	125	79.1	20.9	44.6
	50	31.8	68.2	23.9
	1	85.6	14.4	29.5
	0.5	83.6	16.4	17.2
1 hr	1000	86.9	13.1	96.3
	500	85	15	93.3
	250	65.5	34.5	82.1
	125	85.8	14.2	77.6
	50	93.4	6.65	68.7
	1	92.6	7.44	15.5
	0.5	93.1	6.88	11
2 hrs	1000	70.4	15.4	96.8
	500	60	40	92.9
	250	56.8	43.2	85.1
	125	64.5	35.5	72.3
	50	95.1	4.89	68.1
	1	84.6	15.4	10.7
	0.5	81.7	18.3	13.2

References

- Adams, M.L., Lavasanifar, A., Kwon, G.S. (2003). "Amphiphilic block copolymers for drug delivery." J Pharm Sci **92**: 1343-1355.
- Afonso, N., Bouwman, D. (2008). "Lobular carcinoma in situ." Euro J Canc Prev **17**: 312-316.
- Ashley, C. E., Carnes, E.C., Elper, K.E., Padilla, D.P., Phillips, G.K., Castillo, R.E., Wilkinson, D.C., Wilkinson, B.S., Burgard, C.a., Kalinich, R.M., Townson, J.L., Chackerian, B., Willman, C.L., Peabody, D.S., Wharton, W., Brinker, J.C. (2012). "Delivery of Small Interfering RNA by Peptide-Targeted Mesoporous Silica Nanoparticle-Supported Lipid Bilayers." ACS NANO **6**(3): 2174-2188.
- Ashley, C. E., Carnes, E.C., Phillips, G.K., Padilla, D., Durfee, P.N., Brown, P.A., Hanna, T.N., Liu, J., Phillips, B., Carter, M.B., Carroll, N.J., Jiang, X., Dunphy, D.R., Willman, C.L., Petsev, D.N., Evans, D.G., Parikh, A.N., Chackerian, B., Wharton, W., Peabody, D.S., Brinker, J. (2011). "The targeted delivery of multicomponent cargos to cancer cells by nanoporous particle-supported lipid bilayers." Nature Materials **10**: 389-397.
- Auffray, C., Sieweke, M.H., Geissmann, F. (2009). "Blood monocytes: development, heterogeneity, and relationship with dendritic cells." Annu. Rev. Immunol. **27**: 669-692.
- Bae, Y. H., Park, K. (2011). "Targeted drug delivery to tumors: myths, reality, and possibility." J.Controlled Release **153**: 198-205.
- Balkwill, F. R., Mantovanib, A. (2012). "Cancer-related inflammation: Common themes and therapeutic opportunities." Seminars in Cancer Biology **22**: 33-40.
- Barreto de Melo Rêgo, M.J., Viera de Mello, G.S., André da Silva Santos, C., Chammas, R., Beltrão, E.I. (2013) "Implications on glycobiological aspects of tumor hypoxia in breast ductal carcinoma in situ." Med. Mol. Morphol. **46**: 92-96.
- Batrakova, E. V., Gendelman, H.E., Kabanov, A.V. (2011). "Cell-Mediated drug delivery." Expert Opin. Drug Deliv **8**(4): 415-433.
- Batrakova, E. V., Gendelman, H.E., Kabanov, A.V. (2011). "Cell-Mediated drugs delivery." Expert Opin. Drug Deliv **8**(4): 415-433.
- Carroll, N. J., Pylypenko, S., Atanassov, P.B., Petsev, D.N. (2009). "Microparticles with bimodal nanoporosity derived by microemulsion templating." Langmuir **25**: 13540-13544.

Cheng, C. J., Saltzman, M.W. (2012). "Nanomedicine: downsizing tumor therapeutics." Nature Nanotechnology **7**: 346-347.

Chioda, M., Peranzoni, E (2011). "Myeloid cell diversification and complexity: an old concept with new turns in oncology." Cancer Metastasis Rev. **30**: 27-43.

Choi, M. R., Stanton-Maxey, K.J., Stanley, J.K., Levin, C.S., Bardhan, R., Akin, D., Badve, S., Sturgis, J., Robinson, J.P., Bashir, R., Halas, N.J., Clare, S.E. (2007). "A cellular Trojan Horse for delivery of therapeutic nanoparticles to tumors." Nanno Lett. **7**(12): 3759-3765.

MD Consult. (2000). "Breast Cancer: What is Breast Cancer?". from <http://ylb1.bol.ucla.edu/Pathophysiology.htm>.

Cortez-Retamozoa, V., Etzrodt, M., Newton, A., Rauch, .P.J, Chudnovskiy, A., Berger, C., Ryan, R., Iwamoto, Y., Marinelli, B., Gorbato, R., Forghani, R., Novobrantseva, T.I., Koteliensky, V., Figueiredo, J., Chen, J.W., Anderson, D.G., Nahrendorf, M.N., Swirski, F.K., Weissleder, R., Pittet, M.J. (2012). "Origins of tumor-associated macrophages and neutrophils." PNAS: 1-6.

Danilin, S., Merkel, A.R., Johnson, J.R., Johnson, R.W., Edwards, J.R., Sterling, J.A. (2012). "Meyloid-derived suppressor cells expand during breast cancer progression and promote tumor-induced bone destruction." Oncolmunology **1**(9): 1484-1494.

Dassie, J. P., Giangrande, P.H. (2013). "Current progress on aptamer-targeted olionucleotide therapies." Thermal Delivery **4**(12): 1527-1546.

Dewanjee, M. K., Rao, S.A., Didshelm, P. (1981). "Indium-111 tropolone, a new high-affinity platelet label: preparation and evaluation of labeling parameters." J Nucl Med. **22**: 981-987.

Engberink, R. D., van der Pol, S., deVries, H.E., Blezer, E.L. (2007). "Comparison of SPIO and USPIO for in vitro labeling of human monocytes: MR detection and cell function." Radiology **243**(2): 467-474.

Fisher, D., Francis, G.E., Rickwood, D. (1998). Cell separation: a practical approach, Oxford University Press.

Fluck, M.M, Schaffhausen, B.S. (2009). "Lessons in signaling and tumorigenesis from polyomavirus middle T antigen." Micro and Molec Bio Rev **73**(3): 542-563.

Gbadamosi, J.K., Hunter, A.C., Moghimi, S.M. (2002). "PEGylation of microspheres generates a heterogeneous population of particles with differential surface characteristics and biological performance." FEBS Lett **532**(3): 338-344.

Gutkin, D. W., Shurin, M.R. (2014). "Clinical evaluation of systemic and local immune responses in cancer: time for integration." Cancer Immunol. Immunother. **63**(1): 45-57.

Harake, M. D., Maxwell, A.J., Sukumar, S.A. (2001). "Primary and metastatic lobular carcinoma of the breast." Clinical Radiology **15**(8): 621-630.

Hume, D.A., Ross, I.L., Himes, S.R., Sasmono, R.T., Wells, C.A., Ravasi, T. (2002). "The mononuclear phagocyte system revisited." J Leukoc Biol **72**: 621-627.

Juliano, R.L., Stamp, D. (1975). "The effect of particle size and charge on the clearance rates of liposomes and liposome encapsulated drugs." Biochem Biophys Res Commun **63**: 651-658.

Katrin, K., Hoogenboom, R., Fischer, D., Schubert, U.S. (2010). "Poly(ethylene glycol) in Drug Delivery: Pros and Cons as Well as Potential Alternatives." Angew. Chem. Int. Ed. **49**: 6288-6308.

Kelly, C., Jefferies, C., Cryan, S. (2011). "Targeted liposomal drug delivery to monocytes and macrophages." J. Drug Deliv. **2011**: 1-11.

Kim, T.Y., Kim, D.W., Chung, J.Y., Shin, S.G., Kim, S.C., Heo, D.S., Kim, N.K., Bang, Y.J. (2004). "Phase I and pharmacokinetic study of Genexol-PM, a cremophor-free, polymeric micelle-formulated paclitaxel, in patients with advanced malignancies." Clin Cancer Res **10**: 3708-3716.

Kobayashi, H., Watanabe, R., Choyke, P.L. (2014). "Improving conventional enhanced permeability and retention (EPR) effects; what is the appropriate target?" Theranostics **4**(1): 81-89.

Kruisbeek, A., Ed. (2001). Current Protocols in Immunology: Isolation of mouse mononuclear cells, Wiley Online Library.

Lakhani, S. R., Ellis, I.O., Schnitt, S.J., Tan, P.H., van de Vijver. (2012). WHO classification of tumours of the breast.

Larsen, A.K., Escargueil, A.E., Skladanowski A. (2000). "Resistance mechanisms associated with altered intracellular distribution of anticancer agents." Pharmacol Ther **85**: 217-219.

Leckband, D.E., Kuhl, T.L., Wang, H.K., Müller, W., Herron, J., Ringsdorf, H. (2000). "Direct Force Measurements of Antibody-Antigen Interactions." Methods **20**: 329-340.

Lee, K.D., Hong, K., Papahadjopoulos D. (1992). "Recognition of liposomes by cells: in vitro binding and endocytosis mediated by specific lipid headgroups and surface charge density." Biochim Biophys Acta **1103**(2): 185-197.

Leek, R.D., Lewis, C.E., Whitehouse, R., Greenall, M., Clarke, J., Harris, A.L. (1996). "Association of macrophage infiltration with angiogenesis and prognosis in invasive breast carcinoma." Cancer Research **56**(20): 4625-4629.

Lewis, C. E., Pollard, J.W. (2006). "Distinct role of macrophages in different tumor microenvironments." Cancer Research **66**(2): 605-612.

Lin, E. Y., Jones, J.G., Li, P., Zhu, L., Whitney, K.D., Muller, W.J, Pollard, J.W. (2003). "Progression to malignancy in the polyoma middle T oncoprotein mouse breast cancer model provides a reliable model for human diseases." American J Path **163**(5): 2113-2126.

Markman, M. (2006). "Pegylated liposomal doxorubicin in the treatment of cancers of the breast and ovary." Expert Opin Pharmacother **7**: 1469-1474.

Movahedi, K., Lau, D., Gysemans, C., Baeten, M., Strange, G., Van den Bossche, J., Mack, M., Pipeleers, D., In't Veld, P., De Baetselier, P.D., Van Ginderachter, J.A. (2010). "Different tumor microenvironments contain functionally distinct subsets of macrophages derived from Ly6C(high) monocytes." Cancer Research **70**(14): 5728-5739.

Nakada, D., Oguro, H., Levi, B.P., Ryan, N., Kitano, A., Saitoh, Y., Takeichi, M., Wendt, G.R., Morrison, S.J. (2014). "Oestrogen increases haematopoietic stem-cell self-renewal in females and during pregnancy." Nature Letter **505**: 555-558.

Nowacek, A.S., Miller, R., McMillan, J., Kanmogne, G., Kanmogne, M., Mosley, R.L., Ma, Z., Graham, S., Chaubal, M., Werling, J., Rabinow, B., Dou, H., Gendelman, H.E. (2009). "NanoART synthesis, characterization, uptake, release and toxicology for human monocyte-macrophage drug delivery." Nanomedicine (Lond) **4**(8): 903-917.

Ohno, J., Tajima, Y., Utsumi, N. (1986) "Binding of wheat germ agglutinin in the matrix of rat tracheal cartilage." The Histochemical Journal. **18**(10): 537-540.

Papaldo, P., Fabi, A., Ferretti, G., Mottolese, M., Cianciulli, A.M., Di Cocco, B., Pino, M.S., Carlini, P., Di Cosimo, S., Sacchi, I., Sperduti, I., Nardoni, C., Cognetti, F. (2006). "A phase II study on metastatic breast cancer patients treated with weekly vinorelbine with or without trastuzumab according to HER2 expression: changing the natural history of HER2-positive disease." Ann. Oncol. **17**(4): 630-636.

Polyak, K. (2011). "Heterogeneity in breast cancer." J. Clin. Invest **121**(10): 3786-3788.

Prabhakar, U., Maeda, H., Jain, R.K., Sevick-Muraca, E.M., Zamboni, W., Farokhzad, O.C., Barry, S.T., Gabizon, A., Grodzinski, P., Blakey, D.C. (2013). "Challenges and key considerations of the enhanced permeability and retention (EPR) effect for nanomedicine drug delivery in oncology." Cancer Research **73**(8): 2412-2417.

Rivera, E. (2003). "Current status of liposomal anthracycline therapy in metastatic breast cancer." Clin Breast Cancer **4**: S76-83.

Russo, J., Tay, L.K., Russo, I.H. (1982). "Differentiation of the mammary gland and susceptibility to carcinogenesis." Breast Cancer Research & Treatment **2**: 5-73.

Narayanan S. (1994). "Sialic acid as a tumor marker." Ann Clin Lab Sci **24**(4): 376-334.

Sanna, V., Pala, N., Sechi, M. (2014). "Targeted therapy using nanotechnology: focus on cancer." Int. J. Nanomedicine **15**(9): 467-483.

Siziopikou, K. P. (2013). "Ductal carcinoma in situ of the breast: current concepts and future directions." Arch Pathol Lab Med **137**(4): 462-466.

Sliwkowski, M. X., Mellman, I. (2013). "Antibody therapeutics in cancer." Science **13**(341(6151)): 1192-1198.

Solito S., Falisi, E., Diaz-Montero, C.M., Doni, A., Pinton, L., Rosato, A., Francescato, S., Basso, G., Zanovello, P., Onicescu, G., Garrett-Mayer, E., Montero, A.J., Bronte, V., Mandruzzato, S. (2011). "A human promyelocytic-like population is responsible for the immune suppression mediated by myeloid-derived suppressor cells." Blood **118**(8): 2254-2265.

Söllner T, Bennett, M.K., Whiteheart, S.W., Scheller, R.H., Rothman, J.E. (1993). "A protein assembly-disassembly pathway in vitro that may correspond to sequential steps of synaptic vesicle docking, activation, and fusion." Cell **75**(3): 409-418.

Strebhardt, K., Ullrich, A. (2008). "Paul Ehrlich's magic bullet concept: 100 years of progress." Nat Rev Canc **8**: 473-480.

Talmadge, J. E., Donkor, M., Scholar, E. (2007). "Inflammatory cell infiltration of tumors: Jekyll or Hyde." Cancer Metastasis Rev. **26**(3-4): 373-400.

Terrasse, V., Gaudin, N. (2013). "Latest world cancer statistics: global cancer burden rises to 14.1 million new cases in 2012." International Agency for Research on Cancer.

Vargo-Gogola, T., Rosen, J.M. (2007). "Modelling breast cancer: one size does not fit all." Nature Reviews Cancer **7**: 659-672.

Varki, A., Kannagi, R., Toole, B.P. (2009) "Glycosylation Changes in Cancer." Cold Spring Harbor Laboratory Press (Cold Spring Harbor NY). Chapter 44.

Varmus, H. (2013). "Cancer Research Funding." from <http://www.cancer.gov/cancertopics/factsheet/NCI/research-funding>.

Visvader, J. E. (2009). "Keeping abreast of the mammary epithelial hierarchy and breast tumorigenesis." Genes & Development **25**: 2563-2577.

Wang, S., Yuhui, Y., Liao, L., Kuang, S., Tien, J., O'Malley, B.W., Xu, J. (2009). "Disruption of the SRC-1 gene in mice suppresses breast cancer metastasis without affecting primary tumor formation." PNAS **106**(1): 151-156.

Wynn, T. (2013). "Myeloid differentiation redefined in cancer." Nature Immunology **14**(3): 197-199.

Zhou, Y. (2013). "Ultrasound-mediated drug/gene delivery in solid tumor treatment." J. Healthcare Eng. **4**(2): 223-254.

Zucker-Franklin, D. (1974). "The percentage of monocytes among "mononuclear" cell fractions obtained from normal human blood." J Immunol **112**(1): 234-240.